Droplet migration characteristics in confined oscillatory microflows

Kaustav Chaudhury, Shubhadeep Mandal, and Suman Chakraborty*
Department of Mechanical Engineering, Indian Institute of Technology Kharagpur, Kharagpur-721302, India
(Received 15 July 2015; revised manuscript received 14 January 2016; published 8 February 2016)

We analyze the migration characteristics of a droplet in an oscillatory flow field in a parallel plate microconfinement. Using phase field formalism, we capture the dynamical evolution of the droplet over a wide range of the frequency of the imposed oscillation in the flow field, drop size relative to the channel gap, and the capillary number. The latter two factors imply the contribution of droplet deformability, commonly considered in the study of droplet migration under steady shear flow conditions. We show that the imposed oscillation brings an additional time complexity in the droplet movement, realized through temporally varying drop shape, flow direction, and the inertial response of the droplet. As a consequence, we observe a spatially complicated pathway of the droplet along the transverse direction, in sharp contrast to the smooth migration under a similar yet steady shear flow condition. Intuitively, the longitudinal component of the droplet movement is in tandem with the flow continuity and evolves with time at the same frequency as that of the imposed oscillation, although with an amplitude decreasing with the frequency. The time complexity of the transverse component of the movement pattern, however, cannot be rationalized through such intuitive arguments. Towards bringing out the underlying physics, we further endeavor in a reciprocal identity based analysis. Following this approach, we unveil the time complexities of the droplet movement, which appear to be sufficient to rationalize the complex movement patterns observed through the comprehensive simulation studies. These results can be of profound importance in designing droplet based microfluidic systems in an oscillatory flow environment.

DOI: 10.1103/PhysRevE.93.023106

I. INTRODUCTION

Droplet based microfluidics has brought in a revolution in modern science and technology, with applications ranging from material transport and active and passive mixing in smart and compact technologies, to cutting edge biophysical applications such as photoinitiated catalyst-initiated polymerization inside droplets, targeted drug delivery, and drug discovery [1–5]. In spite of the apparent diversities in many of these applications, the fundamental scientific challenge often boils down to a comprehensive assessment of the migration characteristics of the droplet in a microconfined flow environment. While the migration pattern of a droplet in the presence of a steady background (extensional, simple shear, Poiseuille, etc.) flow has been studied quite extensively [6–16], investigations of the possible implications of a time-complex flow field in a confined microfluidic environment on the same are relatively scarce.

In contrast to the cases of a steady flow, a time-complex flow field introduces an inertial contribution in the flow environment in addition to the time-complex forcing [17]. The latter is commonly perceived as a time varying imposed pressure gradient. Subsequently, the flow field and the droplet shape both evolve with time along with a time varying inertial response of the droplet. Several studies have been reported in the literature on the dynamics of a droplet in time periodic flow environments [18–24]. However, those studies are mostly concerned with the discrete features in isolation: shape dynamics or hydrodynamic forces or streamwise migration characteristics. In contrast, the combined confluence of the above mentioned factors needs to be taken under consideration for actual representation of the dynamics of the immersed droplet, particularly for lateral migration characteristics.

Here, we present a comprehensive description of the migration characteristics of a droplet in an oscillating flow field, confined between two parallel plates. We employ numerical simulations based on phase field formalism, and concurrent analytical calculations based on a reciprocal identity based paradigm towards developing the consensus. The present analysis, based on imposed oscillating flow, eventually unveils most of the generic and essential intricacies of the dynamics of a confined droplet in a time-complex flow field. Moreover, droplet dynamics within a confined flow environment is a representative of a class of soft-body dynamics within a confined physiological environment [25–27]. Therefore, the present study bears a potential impact on the dynamical features of biological moieties (such as red blood cells, white blood cells, etc.) within a physiological system where the true nature of the flow field is eventually time complex.

II. MODEL PROBLEM

We consider a Newtonian droplet of radius a, with dynamic viscosity η and density ρ, initially submerged into another viscosity and density matched immiscible Newtonian fluid within a parallel plate channel, as shown in Fig. 1. The droplet is placed at a certain distance offset from the channel centerline. The flow within the domain is then imposed by providing an oscillating body force. We carry out the analysis with respect to a Cartesian reference frame fixed to the channel wall, as shown in Fig. 1. Accordingly, the unit vectors are denoted by $\hat{\mathbf{e}}_i$ with i being the corresponding coordinate. The imposed oscillating body force is acting along the x direction.

A. Phase field approach

We use the phase field model for simulating the dynamics of the two-fluid system. Particulars regarding this method are

*suman@mech.iitkgp.ernet.in

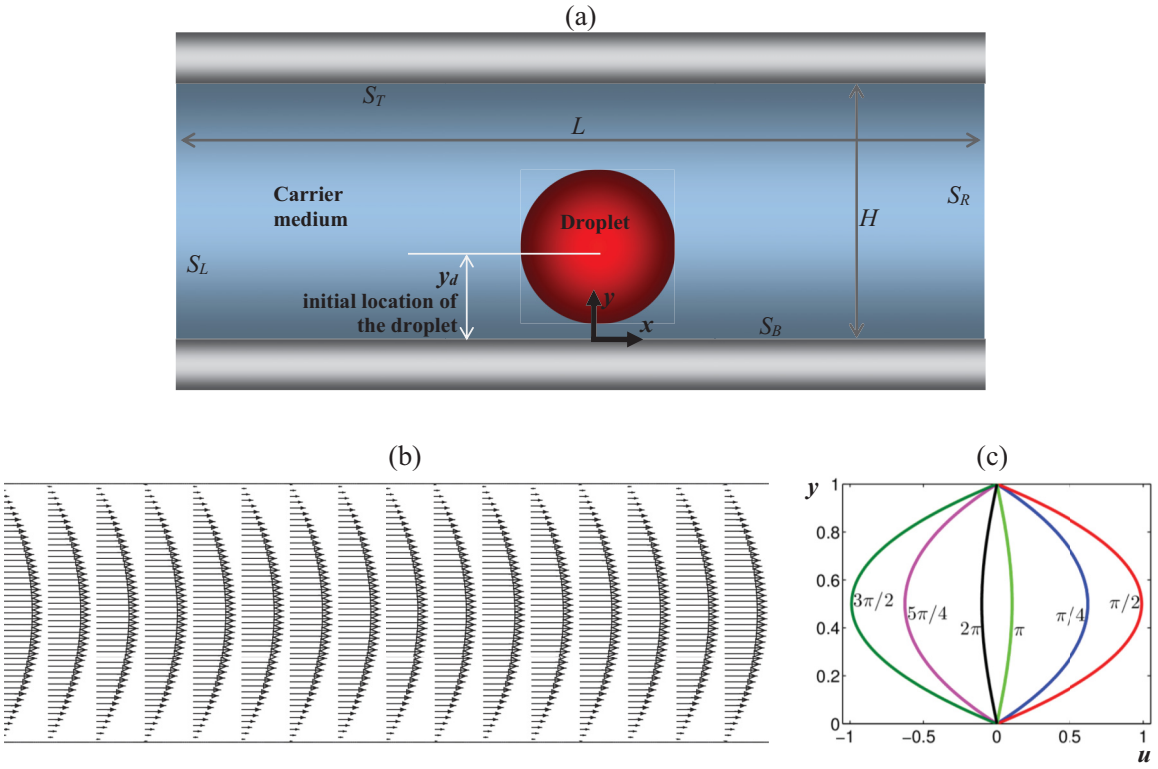

FIG. 1. (a) Model problem setup, showing a Newtonian droplet immersed into another density and viscosity matched immiscible Newtonian carrier fluid, within a parallel plate channel. We consider a rectangular 2D domain of dimensional length L and height H. The domain of computation is bounded by periodically connected left and right boundaries (S_L,S_R), and the top and bottom bounding walls (S_T,S_B). Droplet of initial radius a is placed at a transverse position y_d form the bottom plate. (b) Typical velocity field at $\frac{1}{4}$ of the cycle of imposed forcing; (c) velocity profiles at different stages of the cycle are shown for the sake of comprehensiveness. The profile is shown for the rightmost boundary S_R; however, it remains the same without a droplet at all x.

detailed elsewhere [28–32]. Here we briefly revise the features essential for our study. The distributions of the constituting fluid components are estimated by the distribution of an order parameter $\phi(\mathbf{x},t)$ (with $\mathbf{x}$ and t being position vector and time, respectively), such that $\phi = -1$ denotes the droplet region and $\phi = +1$ denotes the carrier fluid. The interfacial region, between the droplet and the carrier fluid, is given by a diffused zone marked with $-1 < \phi < +1$.

Distribution of $\phi(\mathbf{x},t)$ leads to the free energy distribution $\mathscr{F}(\phi) = \int_\Omega \{f(\phi) + 2^{-1}\sigma\zeta|\nabla\phi|^2\}d\Omega$ over the entire volume of the domain Ω. Here $f(\phi) = 4^{-1}\zeta^{-1}\sigma(\phi^2-1)^2$ represents the bulk free energy density exhibiting minima at the two stable components $\phi = \pm 1$. The $|\nabla\phi|^2$ term inside the integral represents the gradient free energy density, realized over the interfacial zone only. Here, σ and ζ denote the coefficient of surface tension and the characteristic thickness of the diffuse interfacial region, respectively.

The energy principle requires $d\mathscr{F}/dt \leqslant 0$, leading to $(\delta\mathscr{F}/\delta\phi)(d\phi/dt) \leqslant 0$. However, the participating phases for the present situation should be conserved, so that $d\phi/dt = -\nabla\cdot\mathbf{j}$, with $\mathbf{j}$ being the flux vector, for the transport of the order parameter. These considerations lead to the celebrated Cahn-Hilliard equation [28–32]:

$$\frac{\partial\phi}{\partial t} + \mathbf{u}\cdot\nabla\phi = \nabla\cdot(M\nabla\mu). \tag{1}$$

Here $M = M_c(1-\phi^2)$ denotes the interphase mobility factor with M_c as the critical mobility parameter, and $\mu = \delta\mathscr{F}/\delta\phi = \sigma\zeta^{-1}(\phi^3-\phi) - \sigma\zeta\nabla^2\phi$ is the chemical potential.

The velocity field can be obtained from solving the continuity equation

$$\nabla\cdot\mathbf{u} = 0, \tag{2}$$

along with the Navier-Stokes equation

$$\begin{aligned}\frac{\partial}{\partial t}(\rho\mathbf{u}) + \nabla\cdot(\rho\mathbf{u}\mathbf{u}) &= -\nabla p + \nabla\cdot[\eta\{\nabla\mathbf{u} + (\nabla\mathbf{u})^T\}] \\ &\quad - \nabla\cdot\mathbf{T}_S + G_0\sin(\omega t)\hat{\mathbf{e}}_x,\end{aligned} \tag{3}$$

with p as the pressure field. The stress tensor $\mathbf{T}_S$ is due to the interaction between the participating phases [28–30,33]. It is defined as $\mathbf{T}_S = [\partial\mathscr{L}/\partial(\nabla\phi)]\nabla\phi - \mathbf{I}\mathscr{L}$ with $\mathbf{I}$ being the identity tensor, and the Lagrangian $\mathscr{L} = f(\phi) + \sigma\zeta(\nabla\phi)^2/2$ directly follows from the definition of the free energy functional $\mathscr{F}$ and satisfies the Euler-Lagrange equation. For the present consideration, the force of interaction between the participating components eventually simplifies to $-\nabla\cdot\mathbf{T}_S = \mu\nabla\phi$ [28–30,33]. The body force $G_0\sin(\omega t)\hat{\mathbf{e}}_x$ in Eq. (3) delineates the forcing required to maintain the oscillation in the flow field, with G_0 and ω being the amplitude and the frequency, respectively, of the imposed forcing.

Governing equations (1)–(3) are corroborated with the following set of boundary conditions (please refer to Fig. 1 for reference):

At S_T and S_B (with $\hat{\mathbf{n}}_s$ denoting the unit vector normal to a solid surface),

$$\begin{aligned} &\text{(a) } \mathbf{u} - (\mathbf{u}\cdot\hat{\mathbf{n}}_s)\,\hat{\mathbf{n}}_s = \mathbf{0}\,\text{(no slip)},\\ &\text{(b) } \mathbf{u}\cdot\hat{\mathbf{n}}_s = 0\,\text{(no penetration)},\\ &\text{(c) } \hat{\mathbf{n}}_s\cdot\nabla\phi = 0 \text{ and } \hat{\mathbf{n}}_s\cdot\nabla\mu = 0 \;\text{(no flux)}, \end{aligned} \tag{4}$$

and periodic over S_L and S_R, so that

$$\mathbf{u}(\mathbf{x}) = \mathbf{u}(\mathbf{x}+L),\ p(\mathbf{x}) = p(\mathbf{x}+L), \text{ and } \phi(\mathbf{x}) = \phi(\mathbf{x}+L). \tag{5}$$

B. Nondimensional equations and boundary conditions

We conduct the simulation studies over the parametric space of governing nondimensional parameters, to present our analysis in a broad perspective. To this end, we begin with generic scales as follows:

$$\begin{aligned} &\bar{\mathbf{x}} = \frac{\mathbf{x}}{\ell},\quad \bar{\mathbf{u}} = \frac{\mathbf{u}}{U_c},\quad \bar{t} = \frac{t}{\ell/U_c},\quad \bar{p} = \frac{p}{P_c},\\ &\bar{M} = \frac{M}{M_c},\quad \text{and}\quad \bar{\mu} = \frac{\mu}{\mu_c}, \end{aligned} \tag{6}$$

where the quantities at the denominator denote the corresponding scales and the overbar signifies the corresponding normalized quantity. Following Eq. (6), the normalized governing equations, after some arrangements, read as

$$\begin{aligned} &\text{(a) } \bar{\mu} = \left(\frac{\sigma}{\ell\mu_c}\right)\frac{\ell}{\zeta}(\phi^3-\phi) - \left(\frac{\sigma}{\mu_c\ell}\right)\left(\frac{\zeta}{\ell}\right)\bar{\nabla}^2\phi,\\ &\text{(b) } \frac{\partial\phi}{\partial\bar{t}}\left(\frac{\ell}{U_c t_c}\right) + \bar{\mathbf{u}}\cdot\bar{\nabla}\phi = \frac{M_c\mu_c}{U_c\ell}\bar{\nabla}\cdot(\bar{M}\bar{\nabla}\bar{\mu}),\\ &\text{(c) } \bar{\nabla}\cdot\bar{\mathbf{u}} = 0,\\ &\text{(d) } \frac{\rho U_c\ell}{\eta}\left[\frac{\partial\bar{\mathbf{u}}}{\partial\bar{t}}\left(\frac{\ell}{U_c t_c}\right) + \bar{\nabla}\cdot(\bar{\mathbf{u}}\bar{\mathbf{u}})\right]\\ &\quad = -\frac{P_c\ell}{\eta U_c}\bar{\nabla}\bar{p} + \bar{\nabla}\cdot[\{\bar{\nabla}\bar{\mathbf{u}} + (\bar{\nabla}\bar{\mathbf{u}})^T\}]\\ &\qquad + \frac{\mu_c\ell}{\eta U_c}\bar{\mu}\bar{\nabla}\phi + \frac{G_0\ell^2}{\eta U_c}\sin(\omega t_c\bar{t})\hat{\mathbf{e}}_x, \end{aligned} \tag{7}$$

where $\bar{\nabla} = \ell\nabla$. From Eq. (7a) we obtain a natural choice for the scale of chemical potential $\mu_c = \sigma/\ell$. For a phase field based description of droplet dynamics in a given flow field, temporal evolution of the order parameter is primarily governed by the advection of ϕ. Starting from Eq. (7b), this consideration pertains to $O[\partial\phi/\partial\bar{t}(\ell/U_c t_c)] = O[\bar{\mathbf{u}}\cdot\bar{\nabla}\phi]$ or $\ell/U_c t_c = 1$ leading to a choice of time scale $t_c = \ell/U_c$. It is worth mentioning that this choice of t_c is purely based on the requirement from the simulation perspective. In an oscillating flow field, various other times scales are of importance for describing different features [24]. We shall delve into the implications of different time scales, relevant to the present study, *a posteriori* in Sec. IV.

The flow is imposed by a temporally harmonic body force which is essentially acting as an effective pressure gradient. Thus, starting from Eq. (7d), the pertinent balance $O[(P_c\ell/\eta U_c)\bar{\nabla}p] = O[(G_0\ell^2/\eta U_c)\sin(\omega t_c t)\hat{\mathbf{e}}_x]$ or $P_c\ell/\eta U_c = G_0\ell^2/\eta U_c$ is expected to exist. However, a microchannel flow environment is a highly viscous flow condition. Thus, a viscous pressure scale $P_c = \eta U_c/\ell$ is a relevant choice. Following these two balance criteria simultaneously, we have the choice of velocity scale $U_c = G_0\ell^2/\eta$.

Now, if we have a flow through a parallel plate channel driven by a constant pressure gradient of magnitude G_0, the maximum velocity realized at the channel centerline would be $u_{\max} = G_0H^2/8\eta$ where H is the gap height of the channel. The correspondence between these two velocity scales reads as $U_c/u_{\max} = 8(\ell/H)^2$ leading to $O[U_c/u_{\max}] = O[(\ell/H)^2]$. In a time periodic flow environment, the choice of parameters needs to be based on the maximum possible velocity in the domain, towards capturing the features within the full spectrum of the forcing cycle. Thus, it is rational to assume $O[U_c/u_{\max}] = 1$ leading to the modified choice of the characteristic velocity scale $U_c = u_{\max} = G_0H^2/8\eta$.

Following the arguments $O[U_c/u_{\max}] = 1$ and the criterion $O[U_c/u_{\max}] = O[(\ell/H)^2]$, the characteristic length scale appears to be $\ell = H$. In a droplet based system, the radius a of the droplet at initial condition can be another potential choice of length scale, as the characteristic changes occur over this length scale [17,34]. We consider the confined droplet situation where $a/H \in (0,1)$. Under this circumstance, we can assume $O[a/H] = 1$. Thus, choice of either a or H as the characteristic length scale is equivalent. In fact, in several simulation studies [15,35,36], channel dimension is chosen as a characteristic length scale where the simulation results appears to corroborate well with experiment findings. Thus, here we prefer to consider $\ell = H$.

With the above mentioned understanding in the background, the normalized governing equations starting from Eq. (7) read as

$$\begin{aligned} &\text{(a) } \mu = \frac{1}{\mathrm{Cn}}(\phi^3-\phi) - \mathrm{Cn}\nabla^2\phi,\\ &\text{(b) } \frac{\partial\phi}{\partial t} + \mathbf{u}\cdot\nabla\phi = \frac{1}{\mathrm{Pe}}\nabla\cdot(M\nabla\mu),\\ &\text{(c) } \nabla\cdot\mathbf{u} = 0,\\ &\text{(d) } \mathrm{Re}\left[\frac{\partial\mathbf{u}}{\partial t} + \nabla\cdot(\mathbf{u}\mathbf{u})\right]\\ &\quad = -\nabla p + \nabla\cdot[\{\nabla\mathbf{u} + (\nabla\mathbf{u})^T\}]\\ &\qquad + \frac{1}{\mathrm{Ca}}\mu\nabla\phi + 8\sin(t\ \mathrm{St})\hat{\mathbf{e}}_x. \end{aligned} \tag{8}$$

The overbars are dropped, for the sake of convenience; thus the quantities denote their normalized form in Eq. (8). The nondimensional parameters include Péclet number $\mathrm{Pe} = H^2U_c/M_c\sigma$, Reynolds number $\mathrm{Re} = \rho U_cH/\eta$, capillary number $\mathrm{Ca} = \eta U_c/\sigma$, Strouhal number $\mathrm{St} = \omega H/U_c$, Cahn number $\mathrm{Cn} = \zeta/H$, and the relative drop size a/H. The characteristic velocity scale is chosen as $U_c = G_0H^2/8\eta$.

Here Pe denotes the relative importance of the advection of ϕ over the diffusion, as defined through the Cahn-Hilliard equation (1). The appearance of σ in Pe is due to the definition of the free energy functional $\mathscr{F}$ and chemical potential μ using ζ and σ. This is attributed to the connection between

the surface tension with the excess free energy across the interface [28–32]. Among all the parameters discussed above, Cn and Pe are guided by the numerical constraints, to obtain a feasible solution, sufficient to capture the essential features of interest [37–41]. Regarding the remaining parameters, we deliberately keep Re small, so as to mimic common microfluidic applications. We primarily focus on the deformation and the subsequent dynamical features of the droplet, associated with the oscillation in the flow field. Therefore, we vary St (signifying the nondimensional frequency), in addition to Ca and a/H.

C. Implementation

In reference to Fig. 1, we select a two-dimensional (2D) rectangular domain of size (normalized by channel height H) 3×1 which is tessellated with uniform grids. The normalized transport equations [Eq. (8)] are then discretized invoking the finite volume formalism along with semi-implicit time discretization policy. For estimation of the flux functions across the faces of the control volume, we consider a second order upwind scheme. For evaluating all other terms requiring calculation of the values at the faces of the control volumes, a central differencing scheme is employed. We consider the SIMPLE [42] strategy for pressure-velocity coupling. The discretized equations are then solved using the algebraic multigrid (AMG) method [43].

In presenting the results, we consider the migration characteristics given by the droplet position (x_d, y_d) (both normalized by H) and the droplet velocity (u_{dx}, u_{dy}) (both normalized by U_c), as measured along the x and y directions, respectively. Hereinafter, whenever we refer to the mentioned parameters, it should be interpreted as the normalized version, unless otherwise specified. Time t will also be referred to as its normalized version scaled with H/U_c.

III. PHENOMENOLOGICAL FEATURES

The essential physics of droplet migration is characterized by its trajectory, and its longitudinal (axial) and transverse velocity components. With respect to these features, 2D and three-dimensional (3D) simulations at low Reynolds number under steady pressure driven flow condition yield qualitatively similar results. Though a 3D droplet exhibits a slightly higher axial velocity than a 2D droplet, the functional nature of the axial velocity as a function of the axial position remains the same for both cases [15,44]. Thus, the essential physics of droplet migration appears to remain the same for 2D and 3D simulation setups.

It is the hydrodynamic interaction between the droplet and the carrier fluid medium which governs the droplet migration [44]. To this end, the characteristics of the incipient flow field in the presence of the droplet eventually decides this interaction [44,45]. The distribution of the streamlines in a plane passing through the center of a 3D drop is shown to be reminiscent of the flow features captured through 2D simulation. In fact, flow characteristics so obtained from 2D simulations are shown to describe the droplet migration characteristics satisfactorily with respect to experimental observations [44].

A. Plane Poiseuille flow condition and comparison with reported literature

During phase field simulation, spontaneous shrinkage of drop mass or equivalently drop volume for an incompressible fluid can be observed [41]. For a droplet based system, the free energy of the system is concentrated across the two-fluid interfacial region, with zero energy at the bulk. However, the evolution of the participating fluid components in a phase field framework occurs towards minimizing the free energy of the system. Under this circumstance, a possible strategy for energy reduction is by shrinkage of drop volume, tantamount to reducing the interfacial energy. Though volume shrinkage is permissible following the energy minimization principle, it is not acceptable from a practical perspective for a volume conserved system. To tackle this adverse effect of phase field method, we follow the guidelines provided by Feng *et al.* [39,40,38,41].

Volume loss becomes negligible for small interface thickness or equivalently small Cn. Accordingly, we consider two different Cn and the corresponding three different grid sizes to obtain a reasonably small value of Cn, with a motive to achieve minimal loss of volume at computationally affordable expenses. Corresponding interfacial developments are shown in Fig. 2. First, we investigate a parametric space where there is no flow. For $\mathrm{Cn} = 0.02$, we obtain a tanh variation in the phase field order parameter ϕ with x, as shown in Fig. 2(a). This observation is in accordance with fundamental theory of phase field [28,46]. We then observe the drop shape evolution under a steady pressure driven flow environment. Asymptotic steady states of the droplet are shown in Figs. 2(b) and 2(c) for $\mathrm{Cn} = 0.04$ and 0.02 at different grid resolutions. Following the figures, a large reduction of volume of the drop is noted for

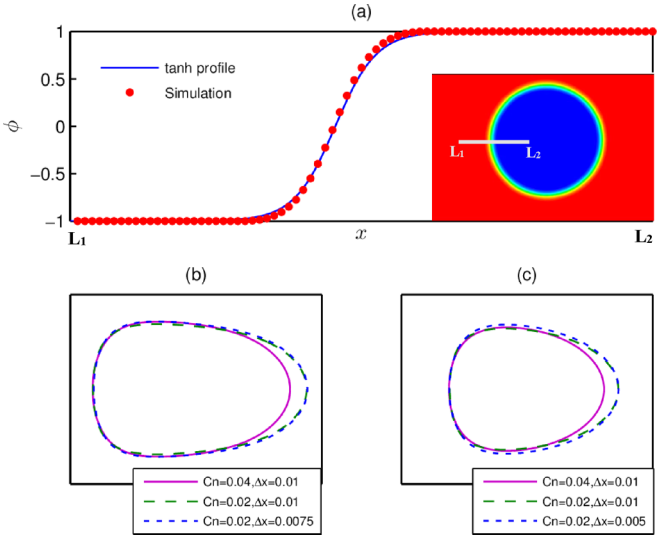

FIG. 2. (a) Variations in the order parameter ϕ with x in the absence of imposed flow compared with the tanh profile at steady state for $a/H = 0.375$, $\mathrm{Ca} = 0.33$, $\mathrm{Cn} = 0.02$, and $\Delta x = 0.01$. The inset represents the contour of the order parameter. (b) Steady state shape of drop in plane Poiseuille flow for $a/H = 0.4375$ and $\mathrm{Ca} = 0.286$. (c) Steady state shape of drop in plane Poiseuille flow for $a/H = 0.375$ and $\mathrm{Ca} = 0.33$. Here we have considered $\mathrm{Re} = 1$.

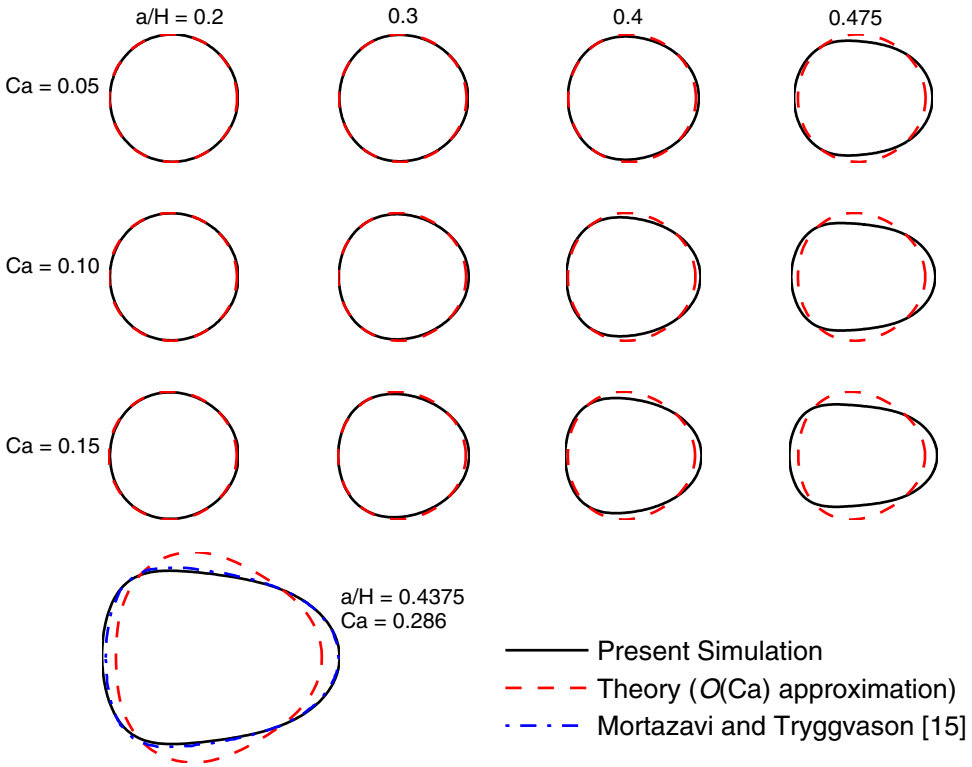

FIG. 3. Characteristic shapes of droplets at different a/H and Ca in plane Poiseuille flow condition, as obtained from the present simulations. For small a/H and Ca, the comparisons are made against the $O(\mathrm{Ca})$ theoretical approximation [Eq. (9)]. For larger droplet ($a/H = 0.4375$) at higher Ca($= 0.286$), the present simulation result is compared against the simulation result of Mortazavi and Tryggvason [15]. Note that here the shapes are shown at 1:1 aspect ratio with axis-tight format. This makes droplets of all sizes to appear as almost the same size, thereby allowing better visualization of the droplets with small a/H. However, the actual sizes of the droplets are in accordance with the respective a/H.

$\mathrm{Cn} = 0.04$. However, with $\mathrm{Cn} = 0.02$, we find that the change in drop volume is very small. Previously executed studies have also reported that $\mathrm{Cn} \leqslant 0.02$ is a reasonable choice [40,41]. In fact the results obtained from $\mathrm{Cn} = 0.02$, as we shall see later, match satisfactorily with previously reported results [15] of front-tracking simulation.

In the low Re regime, the shape of a droplet in a plane Poiseuille flow at a given lateral location depends on a/H and Ca, keeping other parameters fixed [11,47–50]. Theoretically, in the limit $\mathrm{Ca} \ll 1$ and $a/H \ll 1$, the drop shape can be given by [11,47–50]

$$\frac{r}{a} = 1 + \mathrm{Ca}\left\{4\left(1 - \frac{y_d}{H}\right)\frac{16+9\lambda}{8+8\lambda}\frac{x'y'}{r^2}\left(\frac{a}{H}\right) + 4\frac{10+11\lambda}{40+40\lambda}\left(\frac{x'}{r} - \frac{5x'y'^2}{r^3}\right)\left(\frac{a}{H}\right)^2 + O\left[\left(\frac{a}{H}\right)^3\right]\right\} + O(\mathrm{Ca}^2), \tag{9}$$

where $x' = x - x_d$, $y' = y - y_d$, and λ denotes the viscosity contrast, defined as the ratio of the dynamic viscosity of the droplet to that of the carrier medium. We restrict our attention to the case $\lambda = 1$. Evidently, the approximation $r/a = 1$ from Eq. (9) is reminiscent of the leading order spherical shape in a low Reynolds number flow. The remaining terms in Eq. (9) demonstrate the deviation from sphericity. The deformation is characterized by the nondimensional numbers Ca and a/H. The former denotes the deformation due to viscous forcing in comparison to the shape preserving capillary forcing. The latter, on the other hand, signifies the contribution from the bounding walls' effect of confinement.

In Fig. 3, we compare our simulation prediction of drop shape with the theoretical estimation through Eq. (9) and with the numerical results of Mortazavi and Tryggvason [15]. From the figure it is evident that a close agreement with the theoretical estimation in the small a/H and low Ca regime is obtained with our simulation setup for grid size (normalized) $\Delta x = 0.0075$ in both x and y directions, with $\mathrm{Cn} = 0.015$ and $\mathrm{Pe} = 3 \times 10^6$. At higher a/H, the wall-induced deformation produces a highly elongated droplet which deviates much from the theoretical approximation in Eq. (9). For larger drops, we find that $\Delta x = 0.01$ with $\mathrm{Cn} = 0.02$ and $\mathrm{Pe} = 10^6$ being sufficient to capture the droplet dynamics, taking both accuracy and computational expenses into consideration. The setup yields a satisfactorily matching with the shape prediction in Ref. [15], as evident from Fig. 3. These predictions are also in qualitative agreement with experimental findings.

The difference between the present simulation and the theory is pronounced at higher a/H due to the strong involvement of wall-induced deformation at higher a/H. To describe the wall-induced deformation, we present the drop shapes and the corresponding streamline patterns for $a/H = 0.4375$ and $\mathrm{Ca} = 0.286$ in Fig. 4. The streamlines are shown with respect to the droplet reference frame. Two

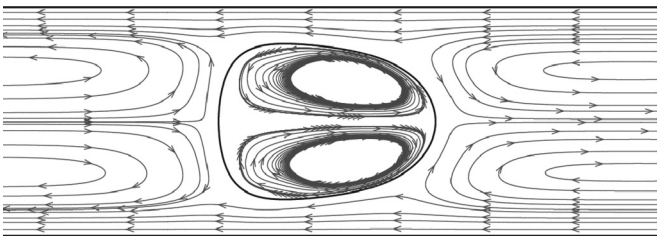

FIG. 4. The distribution of the streamlines, with respect to the droplet reference frame, upon equilibrium settling. The results are shown for $a/H = 0.4375$, with $\mathrm{Re} = 1$ and $\mathrm{Ca} = 0.286$, and the direction of the flow is from left to right, with respect to the figure.

important flow characteristics can be identified: bypass flow near the wall, and recirculating flow within the droplet where the directions of these two flows are mutually opposite. Evidently, with increasing a/H keeping all other parameters fixed, the size of the bypass zone reduces, requiring higher flow rate for bypassing the carrier fluid. Subsequently, to maintain the flow rate balance across the channel cross section, a larger recirculating zone within the droplet with higher flow rate is required. As a result, an elongated droplet (as depicted in Fig. 4) can be observed at higher a/H. In essence, this is the physical aspect behind wall-induced deformation.

It is important to note that two limiting cases are tractable from a theoretical perspective: (i) $a/H \ll 1$ where the drop shape is approximated as a deformed sphere [11], and (ii) $a/H \gg 1$ where the drop shape is approximated by a deformed cylinder with spherical (or deformed spherical) frontal and rear ends [51]. As $a/H \sim 1$, an intermediate drop shape can be observed [45,47,52], as we show in Fig. 4. This intermediate regime is not yet well tractable theoretically, and still poses open ended questions [53].We can only state that the wall-induced deformation produces such elongated shape.

In Fig. 5, we present the temporal evolution of the droplet position $x_d(t)$, $y_d(t)$, and the corresponding migration speeds $u_{dx}(t)$ and $u_{dy}(t)$. Here the results are shown for $a/H = 0.4375$ and 0.375, with $\mathrm{Re} = 1$ and 4, respectively, and $\mathrm{Ca} = 0.286$. This is in accordance with the setup in Ref. [15]. Essentially, this setting gives us an idea about the dynamics of confined droplets. To obtain grid independent results, we have used $\Delta x = 0.01$ with $\mathrm{Cn} = 0.02$ and $\mathrm{Pe} = 10^6$. Starting from the initial position, a droplet always tends to assume a lateral position, from where onwards there will be no acceleration of the droplet, as evident from Fig. 5. This condition is the so-called equilibrium settling of the droplet.

B. Droplet pathway under oscillatory flow condition

The primary knowledge of droplet migration can be obtained from the characteristics of droplet trajectory under the given flow environment. In Fig. 6, we show the trajectories of a droplet under oscillatory flow conditions at different St. The results depict the effect of oscillation, characterized by St, in the background flow field, on the droplet trajectory. Please

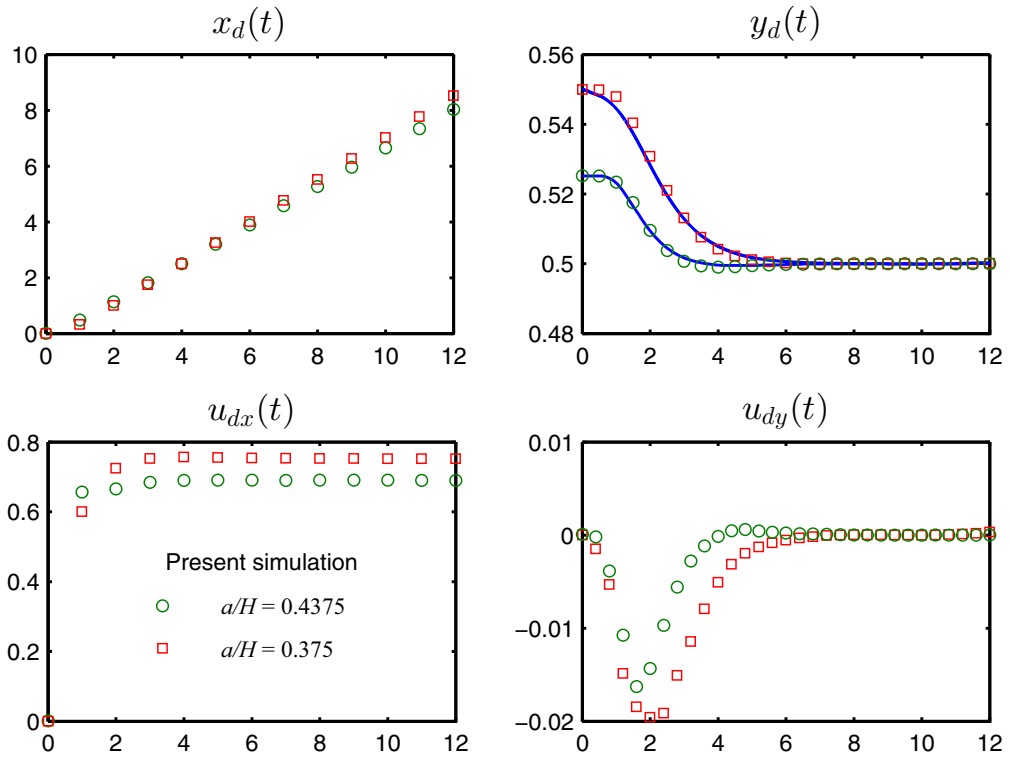

FIG. 5. The time course of the migration characteristics of a droplet in a plane Poiseuille flow condition, for $a/H = 0.4375$ and 0.375 (indicated by the open markers), with $\mathrm{Re} = 1$ and 4, respectively, and $\mathrm{Ca} = 0.286$. The parametric setup is in tune with the setup of Mortazavi and Tryggvason [15]; their results are indicated by the corresponding solid lines. The adopted numerical setup consists of a 2D rectangular domain of dimensionless size length × height = 3 × 1 with grid size $\Delta x = 0.01$. The dimensionless parameters related to the phase field method are taken as $\mathrm{Cn} = 0.02$ and $\mathrm{Pe} = 10^6$.

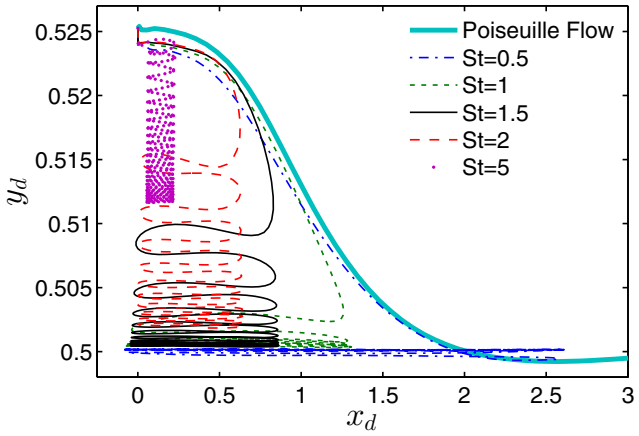

FIG. 6. Trajectory of a confined droplet ($a/H = 0.4375$ and Ca = 0.286) in an oscillating flow field, for different St. The numerical setup corresponds to Cn = 0.02, $\Delta x = 0.01$, and Pe = 10^6, taking accuracy and computational expenses into combined consideration. Please refer to the movie in the Supplemental Material [54] for visual appreciation of the pathway that the droplet follows.

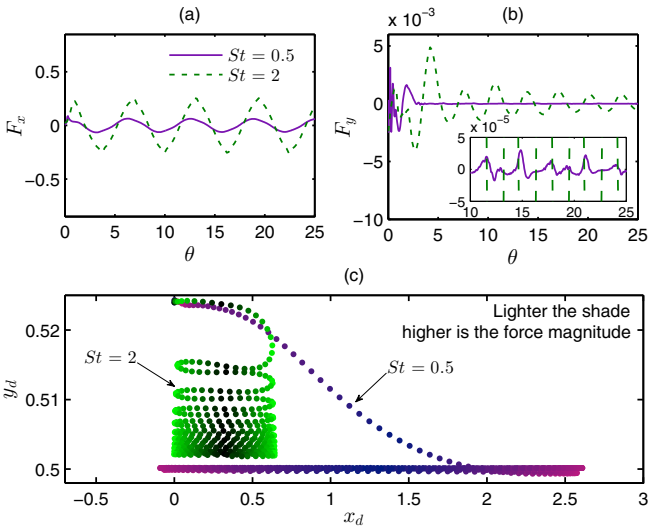

FIG. 7. Temporal and spatial variations in the net force acting on the droplet at two different St. Here, we present the characteristics with respect to $\theta = t\text{St}$, to have a common basis for analysis for different St. Panels (a,b) show the variations in the x and y components, respectively, F_x and F_y of the net force acting on the droplet. Panel (c) describes the force magnitudes at different locations (x_d, y_d) of the droplet. The inset in (b) magnifies in the variations in F_y at St = 0.5 for better visualization. The results are shown for the same setup as in Fig. 6.

refer to the movie in the Supplemental Material [54] for visual appreciation of the pathway that the droplet follows. For the sake of comparison, we also present the trajectory of the same droplet under a plane Poiseuille flow condition. The window of St presented in Fig. 6 depicts a small to significant contribution of oscillation on the droplet trajectory.

In the limit of low St, a close approximation of the droplet trajectory can be observed with that under plane Poiseuille flow condition for a considerable transverse extent. In fact, close matching of the trajectories at St = 0.5 and under plane Poiseuille flow condition can be observed up to the channel centerline, which is eventually the transverse equilibrium location. However, a characteristic oscillatory motion parallel to the channel walls is noteworthy under oscillatory flow condition. From Fig. 6 it also appears that (at least for low) the motion in the transverse direction mainly takes place when the flow switches direction or u_{dx} is smallest in course of sinusoidal variation.

With increasing St, we note from Fig. 6 that there is a progressive deviation of the droplet trajectory from that under plane Poiseuille flow condition. Subsequently, the axial oscillation of the droplet trajectory commences prior to reaching the channel centerline. At the same time, transverse displacement of the droplet takes place without any considerable displacement along the axial direction (cf. the case at St = 5 in Fig. 6). This is of immense significance in practical cases where one tries to move the droplet towards a particular transverse location, but is constrained by the axial extent of the channel. Interestingly, the transverse extent traversed by the droplet progressively reduces with increasing St, even after a considerable amount of the cycle of the imposed oscillation. The observation signifies that oscillation impedes the motion along both axial and transverse directions.

Appreciation of the above mentioned movement characteristics can be obtained from the forcing history on the droplet. Figure 7 shows the temporal and spatial variations in the net force acting on the droplet. The results are shown with respect to $\theta = t\text{St}$, to have a common basis for analysis at different St. Here we specifically show the cases for St = 0.5 and 2, to highlight the comparisons and contrasts at the low and high frequencies of the imposed forcing. Periodic oscillation in F_x [Fig. 7(a)] can be conceptualized through the periodic variation of the imposed forcing along x. However, an oscillatory characteristic in F_y is also noteworthy [Fig. 7(b)]. This leads to the transverse oscillation of the droplet. The oscillation in F_y is more prominent at higher frequency [cf. case St = 2 in Fig. 7(b)]. The F_y oscillation is also present in the case of low frequency case, however, with lower magnitude [cf. inset in Fig. 7(b)].

An interesting insight can be obtained from the spatial variations in the magnitude of the net force at different locations of the droplet (x_d, y_d), as shown in Fig. 7(c). Here the force magnitudes are demonstrated through the shades. The lighter the shade, the higher is the force magnitude. For both the cases, the droplet commences movement with higher magnitude of the net force and progressively encounters forces of low magnitudes. However, a strong forcing confluence is noteworthy while the droplet switches direction of movement. This is evident for both high and low St. This switching is in accordance with the high magnitude situation of the imposed harmonic forcing over the period of variation. It is interesting to note that transverse movement is instigated mostly during these switching instances. Furthermore, the movement of the droplet is impeded at higher St, despite having higher magnitudes of the forces along both directions. This issue will be discussed at length in Sec. IV (Scaling arguments). Prior to that further detailing on the movement characteristics of the droplet is required.

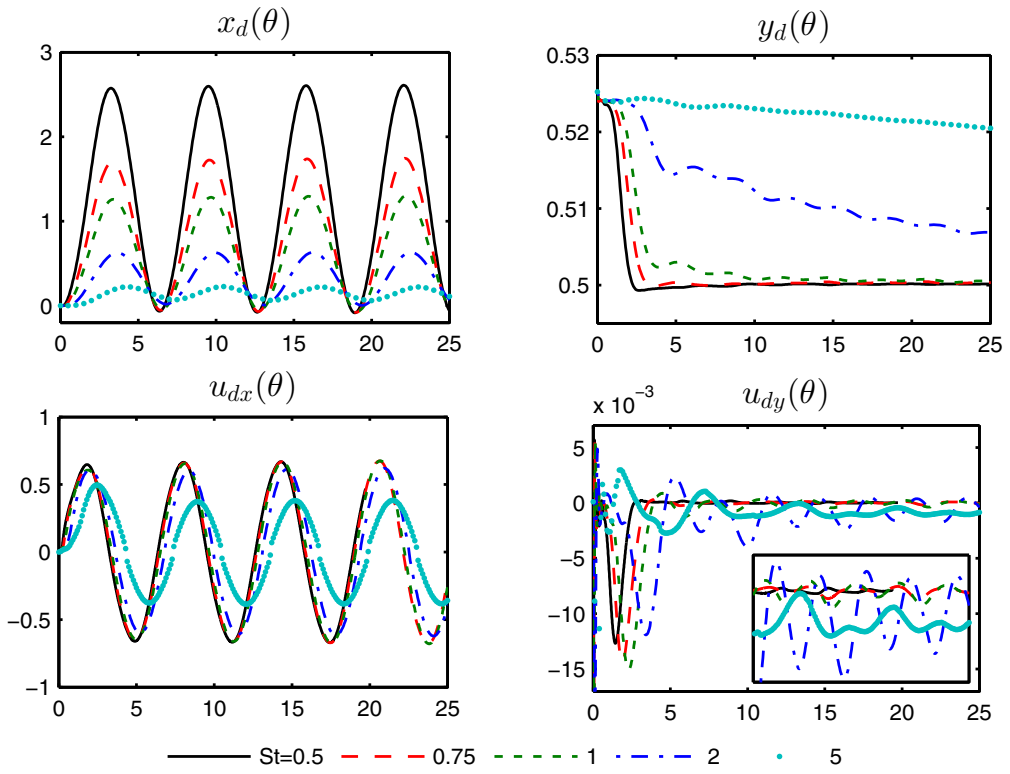

FIG. 8. Characteristics of the pathway of a droplet with $a/H = 0.4375$, Re $= 1$, and Ca $= 0.286$, in an oscillating flow field at different St. Corresponding grid independent and Cn independent studies are presented in the Appendix. The inset in $u_{dy}(\theta)$ magnifies the domain $\theta = 10$ to 25, for clarity.

To unveil the characteristics of the complex movement in detail, it is imperative to consider the temporal evolution characteristics $x_d(t)$, $y_d(t)$, $u_{dx}(t)$, and $u_{dy}(t)$ (the latter two are the respective components of the droplet velocity). Figure 8 demonstrates those characteristics, for Ca $= 0.286$, Re $= 1$, and $a/H = 0.4375$. From Fig. 8 it appears that unlike the plane Poiseuille flow condition, here $x_d(\theta)$ and $u_{dx}(\theta)$ both follow an oscillating nature. This behavior seems intuitive, and can be attributed to the change in momentum along the x direction due to the oscillating body force acting along the same direction. However, the oscillating pattern in the transverse migration characteristics $y_d(\theta)$ and $u_{dy}(\theta)$, as can be seen in Fig. 8, is difficult to rationalize by such a simple argument.

From the $u_{dx}(\theta)$ variations in Fig. 8, it appears that St has little impact on u_{dx}, at least in the low St regime. However, in the $x_d(\theta)$ characteristics, we note a decreasing trend of the amplitude of x_d with St. Additionally, in Fig. 8, we also observe the oscillating nature of the transverse migration characteristics $y_d(\theta)$ and $u_{dy}(\theta)$ at all St values considered here. Nevertheless, a net lateral migration from the initial position is noteworthy.

The imposed oscillatory forcing exhibits sinusoidal variations in time as $\psi = \sin(t\text{St})$. Accordingly, u_{dx} and u_{dy} are the response of the droplet. It is therefore prudent to analyze the interrelationship between ψ, u_{dx}, and u_{dy}. The interrelationships are shown in Fig. 9. The figures resemble Lissajous-like figures, demonstrating the correlation between two harmonic functions. Here we show the results for (a) St $=$ 0.75, (b) St $= 1$, and (c) St $= 3$, reminiscent of low, moderate, and high frequency regimes of imposed forcing, respectively.

From all the cases, an elliptical relationship between ψ and u_{dx} can be identified. Following this elliptical pattern, we can identify sinusoidal temporal variation of u_{dx} with frequency St, similar to that of the imposed forcing. However, a distortion in the elliptical pattern is noted at the high frequency regime (cf. the case St $= 3$). This is attributed to the faster change in the imposed oscillation in comparison to the time scale of transportation (discussed in detail in Sec. IV). However, the patterns depicted by the figures of $\psi - u_{dy}$ and $u_{dx} - u_{dy}$ cannot be formalized by any simple functional form of u_{dy}.

C. Morphological characteristics under oscillatory flow condition

Deformability of a droplet is considered to be one of the prime contributors to the cross-stream migration characteristics. In Fig. 10, we show the migration characteristics for St $= 1$ at different Ca [Fig. 10(a)] and a/H [Fig. 10(b)] values. In the small a/H and low Ca limit, droplet deformation is expected to be small. From Fig. 10 it is evident that under such condition, transverse oscillation still persists. Thus, it appears that oscillation in the $y_d(\theta)$ and $u_{dy}(\theta)$ characteristics is an inherent feature that is associated with the oscillation in the imposed flow field.

Further elucidation on the droplet morphology can be obtained from the temporal evolution of the droplet perimeter Γ [55], for the 2D setup considered here. Figure 11(a) shows the evolution of Γ (normalized by the initial perimeter of the droplet) under oscillatory flow environment at St $= 1$.

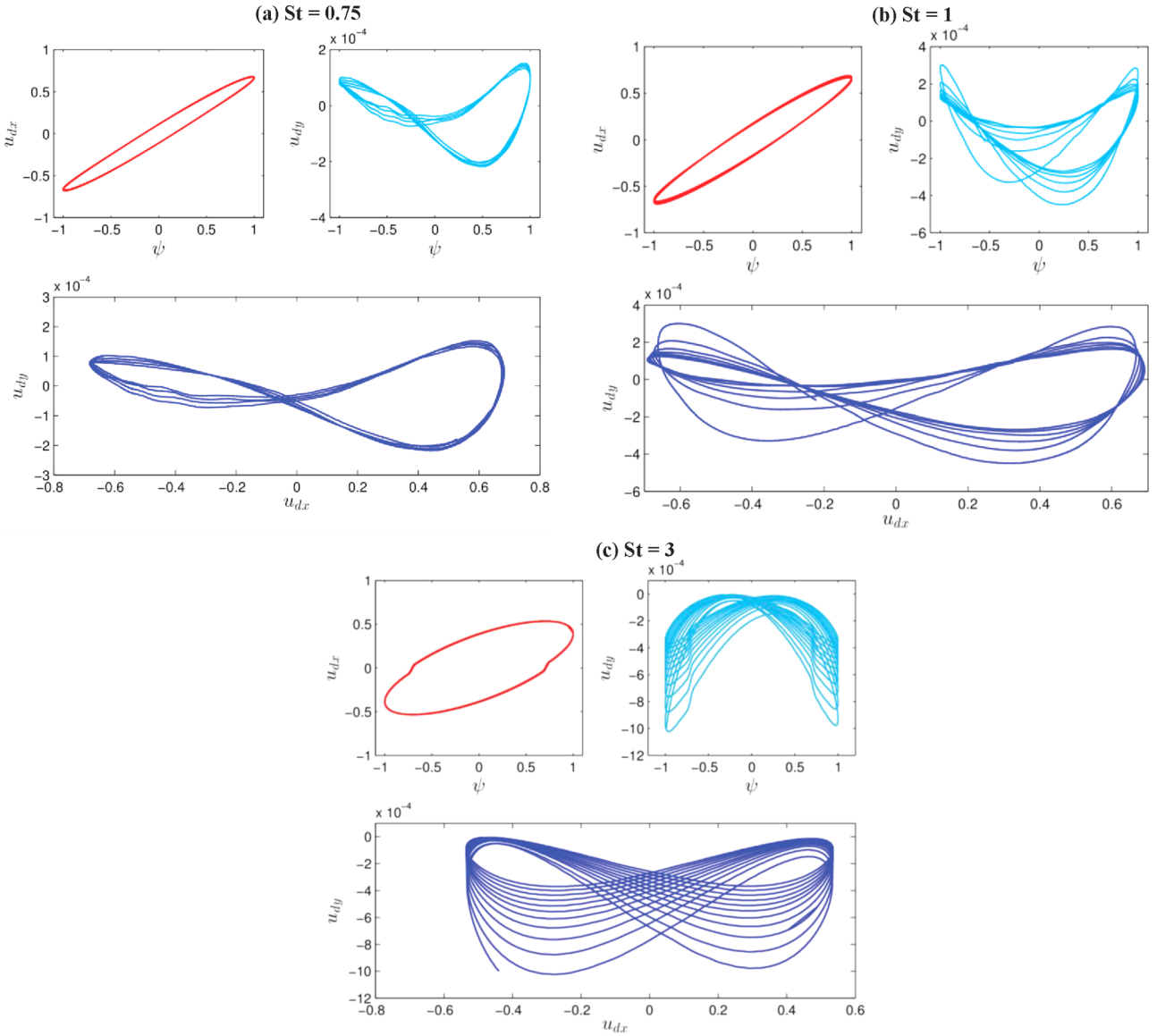

FIG. 9. Variations in drop velocities (u_{dx},u_{dy}) with the imposed forcing (ψ) for (a) St = 0.75, (b) St = 1, and (c) St = 3. Other parameters have the following values: $a/H = 0.4375$, Ca = 0.286, Re = 1, and $y_d = 0.525$.

A comparative assessment of the same at different St is shown in Fig. 11(b). To investigate the physical picture in more detail, we show the drop shapes at different time instants.

We observe the bulletlike shape of the drop in a few time instances which is asymmetric with respect to the lateral direction. As shown in Fig. 11(a), at time instant $t = t_1,t_2$, the drop shape is bulletlike and the nose (narrow end) of the bullet is in the backward direction (flow is from left to right which is termed as forward direction). However, at time instant $t = t_3$ the drop shape becomes almost symmetric with respect to the lateral direction. In later times, the drops deform to bulletlike shapes but with the nose directing in the forward direction (for $t = t_4,t_5$). With due course of time, the drop shapes becomes asymmetric bulletlike (with backward nose), symmetric with respect to the transverse plane, and asymmetric bulletlike (with forward nose). The drop attains these three shapes periodically.

IV. SCALING ARGUMENTS

We have already mentioned that in a time periodic flow, different time scales have different physical implications. This fact can be well understood from the force balance perspective. To this end we begin with the scaled momentum balance equation without any prior choice of ℓ, U_c, and t_c:

$$\underbrace{\frac{\rho U_c}{t_c}\frac{\partial \bar{\mathbf{u}}}{\partial \bar{t}}}_{K_1} + \underbrace{\frac{\rho U_c^2}{\ell}\bar{\nabla}\cdot(\bar{\mathbf{u}}\bar{\mathbf{u}})}_{K_2} = \underbrace{-\frac{P_c}{\ell}\bar{\nabla}\bar{p}}_{K_3} + \underbrace{\frac{\eta U_c}{\ell^2}\bar{\nabla}\cdot[\{\bar{\nabla}\bar{\mathbf{u}} + (\bar{\nabla}\bar{\mathbf{u}})^T\}]}_{K_4} + \underbrace{\frac{\sigma}{\ell^2}\bar{\mu}\bar{\nabla}\phi}_{K_5} + \underbrace{G_0\sin(\omega t_c\bar{t})\hat{\mathbf{e}}_x}_{K_6}. \quad (10)$$

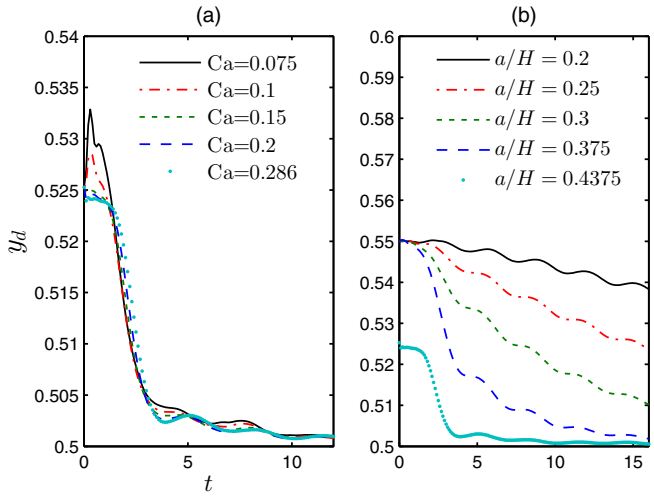

FIG. 10. The migration characteristics of a droplet in an oscillating flow field, for St = 1 at different (a) Ca (keeping $a/H = 0.4375$) and (b) a/H (keeping Ca = 0.286), with Re = 1 for both cases.

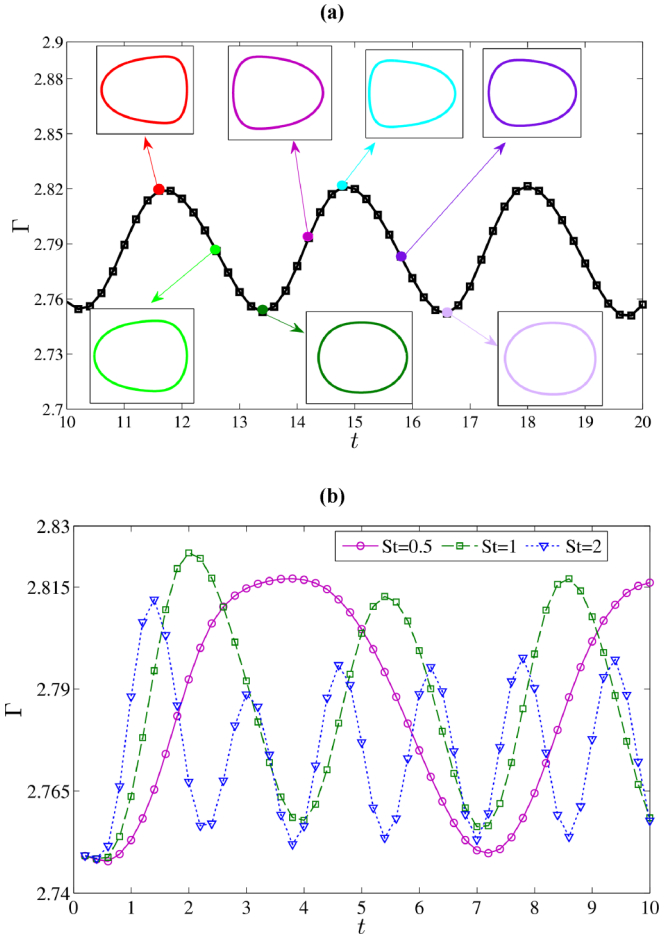

FIG. 11. (a) Variations in drop perimeter and drop shape with time for St = 1. (b) Variation of drop perimeter with time for three different values of St = 0.5, 1, and 2. Other parameters have the following values: $a/H = 0.4375$, Ca = 0.286, $y_d = 0.525$, and Re = 1.

Here we only consider the scale for the chemical potential of the order parameter as $\mu_c = \sigma/\ell$. From Eq. (10) we can have different choices of the time scale, based on different balance criteria and important different physical aspects, as follows:

$$\text{(a) Advection: } O(K_1) = O(K_2) \Rightarrow t_{c,A} = \frac{\ell}{U_c},$$

$$\text{(b) Viscous: } O(K_1) = O(K_4) \Rightarrow t_{c,V} = \frac{\rho \ell^2}{\eta},$$

$$\text{(c) Drop shape modification: O(K}_1\text{)} = \text{O(K}_5\text{)} \Rightarrow t_{c,S} = \frac{\rho \ell^2 U_c}{\sigma}. \tag{11}$$

Evidently, the time scale of imposing the oscillatory forcing is $t_F = 1/\omega$.

In a droplet based system, advection of the submerged droplet is an important requirement. This issue in response to the oscillatory forcing can be understood from the factor $t_{c,A}/t_F = \omega \ell / U_c$ which is essentially St when $\ell = H$ as per present choice of scales. A droplet undergoes transportation when the time scale of altering the imposed forcing t_F is longer (or almost the same, at the most) than the transportation time scale $t_{c,A}$ so that the transportation can be adjusted at every instant. This understanding leads to $t_{c,A}/t_F \leqslant 1$ or St $\leqslant 1$. Thus, at very high St, droplet transportation is expected to be impeded due to the rapid change in the magnitude of and the direction of the oscillatory forcing. In response to the observed trajectories of the droplet at high frequency, depicted through Fig. 6, we note that at high frequency droplet motion is impeded in both axial and transverse direction. The genesis of such behavior can now be appreciated in perspective of the time scale analysis as depicted above.

Towards estimating the drop shape change in response to the imposed time periodic forcing, we need to consider the factor $t_{c,S}/t_F = \omega \rho \ell^2 U_c/\sigma = (\omega \ell/U_c)(\rho U_c \ell/\eta)(\eta U_c/\sigma) = \text{StReCa}$. It is evident that the droplet can have sufficient time to adjust its shape in response to the temporally alternating forcing, if $t_{c,S}/t_F \leqslant 1$, while the equality is the limiting case. Thus, drop shape modification takes place when St $\leqslant (\text{ReCa})^{-1}$. It is worth mentioning, as we shall see in the subsequent section, that the $O(\text{ReCa})$ contribution is the indicator of droplet deformation due to the combined influence of inertia, viscous, and surface tension, encompassing the primary forcing factors in a time periodic flow field.

V. AN ANALYTICAL DESCRIPTION OF DROPLET MOTION

Here our primary goal is to unveil an estimation of the time complexity of $x_d(t)$, $y_d(t)$, $u_{dx}(t)$, and $u_{dy}(t)$ due to the imposed time-complex flow field, leading towards the complex movement of a droplet within a confinement. To this end, we proceed with the reciprocal identity based analysis. Our problem can be generalized as the motion of a viscous droplet of dynamic viscosity $\lambda\eta$ and density ρ in a unidirectional time-complex flow field of an incompressible Newtonian fluid of dynamic viscosity η and density ρ, in between two infinite

parallel plates. Specifically, for the case studies presented in this work, $\lambda = 1$. However, we proceed with the analysis of arbitrary λ, for the sake of completeness.

For theoretical analysis, it is convenient to analyze the situation with respect to the droplet reference frame. However, the position (x_d, y_d) and the velocity $(\mathbf{u}_d)$ (in vector form) of the droplet are measured with respect to the fixed x-y reference frame. Now, we define a Cartesian reference frame ξ-ψ fixed to the droplet where its origin coincides with the droplet centroid, with ξ and ψ aligning parallel to the x and y axes, respectively. Hereinafter, the Cartesian reference frame ξ-ψ will be referred to as the *droplet reference frame*, unless otherwise specified, and the position vector with respect to this frame will be given by $\mathbf{r}$.

In our simulations, we consider that the oscillation in the flow field is imposed by an oscillating body force. For theoretical convenience, here we assume this to be incorporated into the pressure gradient term for the imposed flow field. In accordance with our problem, we consider $\mathrm{Re} = \rho U_c a/\eta \ll 1$. Note that here the characteristic length scale for normalization is a, instead of H (considered for normalization of our simulation model). Other scales for normalization are the same as in our simulation setup. Additionally, here we also consider $\mathrm{Ca} = \eta U_c/\sigma \ll 1$. The small Ca approximation essentially allows analytical tractability, for droplet based problems [11]. Moreover, the theoretical understanding obtained from small Ca based analysis can also be extended to moderate and even sometimes high Ca cases, at least for unveiling the essential features of interest.

Pertaining to the present situation under consideration, the governing equations, in nondimensional form, with respect to the droplet reference frame can be recast as

$$\begin{aligned}
&\text{(a) } \nabla\cdot\mathbf{u} = 0 \text{ and } \nabla\cdot\mathbf{T} = \mathrm{Re}\left(\frac{\partial\mathbf{u}}{\partial t} + \mathbf{u}\cdot\nabla\mathbf{u}\right) \text{with } \mathbf{T} = -p\mathbf{I} + \{\nabla\mathbf{u} + (\nabla\mathbf{u})^T\},\\
&\text{(b) } \nabla\cdot\bar{\mathbf{u}} = 0 \text{ and } \nabla\cdot\bar{\mathbf{T}} = \mathrm{Re}\left(\frac{\partial\bar{\mathbf{u}}}{\partial t} + \bar{\mathbf{u}}\cdot\nabla\bar{\mathbf{u}}\right) \text{with } \bar{\mathbf{T}} = -\lambda\bar{p}\mathbf{I} + \lambda\{\nabla\bar{\mathbf{u}} + (\nabla\bar{\mathbf{u}})^T\},\\
&\text{(c) } \nabla\cdot\mathbf{u}_\infty = 0 \text{ and } \nabla\cdot\mathbf{T}_\infty = \mathrm{Re}\left(\frac{\partial\mathbf{u}_\infty}{\partial t} + \mathbf{u}_\infty\cdot\nabla\mathbf{u}_\infty\right) \text{with } \mathbf{T}_\infty = -p_\infty\mathbf{I} + \{\nabla\mathbf{u}_\infty + (\nabla\mathbf{u}_\infty)^T\},
\end{aligned} \tag{12}$$

for the region (a) outside and (b) inside the droplet, and for the (c) imposed flow field. The velocity, pressure, and stress distributions for the corresponding domains are denoted, respectively, by $(\mathbf{u}, p, \mathbf{T})$, $(\bar{\mathbf{u}}, \bar{p}, \bar{\mathbf{T}})$, and $(\mathbf{u}_\infty, p_\infty, \mathbf{T}_\infty)$. The above equations are coupled with the boundary conditions:

$$\begin{aligned}
&\text{(a) } \mathbf{u} \to \mathbf{u}_\infty \text{ as } r \to \infty \text{ (with } r = |\mathbf{r}|),\\
&\text{(b) } \mathbf{u} = -\mathbf{u}_d \quad \text{on the walls,}
\end{aligned} \tag{13}$$

and interfacial conditions at the surface of the droplet,

$$\begin{aligned}
&\text{(a) } \mathbf{u} = \bar{\mathbf{u}},\\
&\text{(b) } \mathbf{u}\cdot\hat{\mathbf{n}} = \bar{\mathbf{u}}\cdot\hat{\mathbf{n}} = 0,\\
&\text{(c) } \mathbf{T}\cdot\hat{\mathbf{n}} - \bar{\mathbf{T}}\cdot\hat{\mathbf{n}} = \frac{1}{\mathrm{Ca}}\kappa\hat{\mathbf{n}}.
\end{aligned} \tag{14}$$

Here κ denotes the local curvature of the surface of the droplet with $\hat{\mathbf{n}}$ being the unit outward normal.

A. The reciprocal identity

Our theoretical estimation is centered on the reciprocal identity based analysis. In this method, the analysis commences with the consideration of a complementary problem such that the shape of the droplet for the complementary problem and the original problem are same. To this end, we consider the motion of a Newtonian droplet in a density and viscosity matched Newtonian fluid where the droplet is translating perpendicular to the walls of the channel. Accordingly, its flow characteristics outside and inside the droplet are given by $(\mathbf{u}_c, p_c, \mathbf{T}_c)$ and $(\bar{\mathbf{u}}_c, \bar{p}_c, \bar{\mathbf{T}}_c)$, respectively. The governing equations, along with the boundary and interfacial conditions, have standard forms, and adopted here as is [11,17,23,49]. Thus, we prefer not to repeat them again. We must note that the original problem can be reduced by means of domain perturbation to an equivalent spherical droplet case, for applying the interfacial conditions [11,17]. Thus, we may conveniently proceed with the spherical droplet consideration for the complementary problem.

Following the standard procedure of reciprocal based analysis, we eventually end up with the identity of the form

$$\begin{aligned}
&\int_{S_d} [(\mathbf{T} - \bar{\mathbf{T}})\cdot\mathbf{u}_c - (\mathbf{T}_c - \bar{\mathbf{T}}_c)\cdot\mathbf{u} - \bar{\mathbf{T}}_c\cdot(\mathbf{u} - \bar{\mathbf{u}})\\
&\qquad - \mathbf{T}_\infty\cdot\mathbf{u}_c + \mathbf{T}_c\cdot\mathbf{u}_\infty]\cdot\hat{\mathbf{e}}_r dS\\
&= -\mathrm{Re}\left\{\int_\Omega \left[\left(\frac{\partial\mathbf{u}}{\partial t} + \mathbf{u}\cdot\nabla\mathbf{u}\right)\right.\right.\\
&\qquad \left.\left. - \left(\frac{\partial\mathbf{u}_\infty}{\partial t} + \mathbf{u}_\infty\cdot\nabla\mathbf{u}_\infty\right)\right]\cdot\mathbf{u}_c d\Omega\right.\\
&\qquad \left. - \int_\Omega \left[\frac{\partial\bar{\mathbf{u}}}{\partial t} + \bar{\mathbf{u}}\cdot\nabla\bar{\mathbf{u}}\right]\cdot\bar{\mathbf{u}}_c d\Omega\right\},
\end{aligned} \tag{15}$$

where S_d denotes the surface of the droplet and Ω denotes the volume of the entire problem domain. The procedure to arrive at the reciprocal identity is similar to that outlined in Refs. [11,17]. However, here the only difference is the inclusion of the inertial volume integrals, attributable to the time complexity involved with the problem. Similar volume integrals can be observed in Refs. [22,23], dealing with the inertial contribution in droplet dynamics.

B. Asymptotic expansion

Owing to the consideration of small Re and Ca, it is possible to proceed with the double asymptotic expansion [11],

$$A = A^{(0)} + \mathrm{Re}A^{(\mathrm{Re})} + \mathrm{Ca}A^{(\mathrm{Ca})} + \mathrm{Ca}^2 A^{(\mathrm{CaCa})} + \mathrm{ReCa}A^{(\mathrm{ReCa})} + \mathrm{Re}^2 A^{(\mathrm{ReRe})} + \cdots, \tag{16}$$

for any arbitrary function A which can be anything from $\mathbf{u}_d$, $(\mathbf{u}, p, \mathbf{T})$, $(\bar{\mathbf{u}}, \bar{p}, \bar{\mathbf{T}})$, and $(\mathbf{u}_\infty, p_\infty, \mathbf{T}_\infty)$. For $\bar{p}$ and $\bar{\mathbf{T}}$, additionally, we need to consider the $O(\mathrm{Ca}^{-1})$ contribution towards satisfying the Laplace pressure jump [11].

Following the above mentioned approach, the shape of the droplet can be approximated as

$$F \equiv r - 1 - \underbrace{(\mathrm{Ca}f^{(\mathrm{Ca})} + \mathrm{ReCa}f^{(\mathrm{ReCa})} + \mathrm{Ca}^2 f^{(\mathrm{CaCa})} + \cdots)}_{\mathscr{J}(\mathbf{r},t)} = 0, \tag{17}$$

where $\mathscr{J}$ signifies the deviation from sphericity expressed in terms of the yet unknown function f. Note that in expanding $\mathscr{J}$, the first contribution of Re comes from the $O(\mathrm{ReCa})$ term. Actually, the droplet can deform even in the complete absence of inertia, as signified by the $O(\mathrm{Ca})$ contribution. In the presence of inertia, however, the deformation is contributed by the combined influence of Re and Ca. Using F, now we can define

$$\hat{\mathbf{n}} = \frac{\nabla F}{|\nabla F|} = \hat{\mathbf{e}}_r - \mathrm{Ca}\nabla f^{(\mathrm{Ca})} - \mathrm{ReCa}\nabla f^{(\mathrm{ReCa})} - \mathrm{Ca}^2\left[\nabla f^{(\mathrm{CaCa})} + \frac{(\nabla f^{(\mathrm{Ca})} \cdot \nabla f^{(\mathrm{Ca})})\hat{\mathbf{e}}_r}{2}\right] - \cdots, \tag{18}$$

and

$$\kappa = \nabla \cdot \hat{\mathbf{n}} = 2 - \mathrm{Ca}[2f^{(\mathrm{Ca})} + \nabla^2 f^{(\mathrm{Ca})}] - \mathrm{ReCa}[2f^{(\mathrm{ReCa})} + \nabla^2 f^{(\mathrm{ReCa})}] - \mathrm{Ca}^2[2f^{(\mathrm{CaCa})} - 2f^{(\mathrm{Ca})}f^{(\mathrm{Ca})} + \nabla^2 f^{(\mathrm{CaCa})}] - \cdots, \tag{19}$$

with $\hat{\mathbf{e}}_r$ as the unit vector along the radial direction.

C. The case of spherical droplet: the $O(1)$ problem

The governing equations for the $O(1)$ problem are

$$\left.\begin{aligned} &\text{(a) } \nabla \cdot \mathbf{u}^{(0)} = 0 \text{ and } \nabla \cdot \mathbf{T}^{(0)} = 0, \\ &\text{(b) } \nabla \cdot \bar{\mathbf{u}}^{(0)} = 0 \text{ and } \nabla \cdot \bar{\mathbf{T}}^{(0)} = 0, \\ &\text{(c) } \nabla \cdot \mathbf{u}_\infty^{(0)} = 0 \text{ and } \nabla \cdot \mathbf{T}_\infty^{(0)} = 0, \end{aligned}\right\} \tag{20}$$

with the boundary and interfacial conditions

$$\begin{aligned} &\text{(i) } \mathbf{u}^{(0)} \to \mathbf{u}_\infty^{(0)} \text{ as } r \to \infty, \\ &\text{(ii) } \mathbf{u}^{(0)} = -\mathbf{u}_d^{(0)} \text{ on the walls}, \\ &\text{(iii) } \mathbf{u}^{(0)} = \bar{\mathbf{u}}^{(0)} \text{ at } r = 1, \\ &\text{(iv) } \mathbf{u}^{(0)} \cdot \hat{\mathbf{e}}_r = \bar{\mathbf{u}}^{(0)} \cdot \hat{\mathbf{e}}_r = 0 \text{ at } r = 1, \text{ and} \\ &\text{(v) } \mathbf{T}^{(0)} \cdot \hat{\mathbf{e}}_r - \bar{\mathbf{T}}^{(0)} \cdot \hat{\mathbf{e}}_r = -[2f^{(\mathrm{Ca})} + \nabla^2 f^{(\mathrm{Ca})}]\hat{\mathbf{e}}_r \text{ at } r = 1. \end{aligned} \tag{21}$$

Solution for the imposed flow field can be recast as

$$\mathbf{u}_\infty^{(0)} = (\alpha + \beta\psi + \gamma\psi^2)\Gamma(t)\hat{\mathbf{e}}_\xi - \mathbf{u}_d^{(0)}. \tag{22}$$

where $\alpha = 4y_d(1 - y_d)$, $\beta = 4(1 - 2y_d)a/H$, and $\gamma = -4(a/H)^2$. In Eq. (22) $\Gamma(t) = \varepsilon_1 + \varepsilon_2 \sin(t\,\mathrm{St})$ such that $\varepsilon_1 = 1, \varepsilon_2 = 0$ represents the Poiseuille flow condition and $\varepsilon_1 = 0, \varepsilon_2 = 1$ denotes the oscillating flow condition. It is to be noted that for the spherical droplet problem, one can directly adopt the solution proposed by Chan and Leal [11], with the coefficients α, β, and γ of their paper be replaced by $\alpha\Gamma(t)$, $\beta\Gamma(t)$, and $\gamma\Gamma(t)$. We must appreciate that at the $O(1)$ approximation it is possible to estimate $u_{dx}^{(0)} = \mathbf{u}_d^{(0)} \cdot \hat{\mathbf{e}}_x = \mathbf{u}_d^{(0)} \cdot \hat{\mathbf{e}}_\xi$. Additionally, due to aft-fore symmetry, $u_{dy}^{(0)} = \mathbf{u}_d^{(0)} \cdot \hat{\mathbf{e}}_y = \mathbf{u}_d^{(0)} \cdot \hat{\mathbf{e}}_\psi = 0$. Now, proceeding with the notion that the net force acting on the neutrally buoyant droplet is zero, one can obtain

$$u_{dx}^{(0)} = \Lambda_{\mathrm{CL}}\Gamma(t), \tag{23}$$

where $\Lambda_{\mathrm{CL}} = \alpha + \gamma\lambda/(2 + 3\lambda) + I_1 + I_4/2$ represents the same function as given in Ref. [11]. Now, we proceed with the form of $\Gamma(t) = \varepsilon_1 + \varepsilon_2 \sin(t\mathrm{St})$.

For the Poiseuille flow condition ($\varepsilon_1 = 1, \varepsilon_2 = 0$), Eq. (23) degenerates to the form $u_{dx}^{(0)} = \Lambda_{\mathrm{CL}} = \alpha + \gamma\lambda/(2 + 3\lambda) + I_1 + I_4/2$. This is a very popular estimation of streamwise migration speed of a droplet in plane Poiseuille flow. In Sec. III, we have already presented the form $u_{dx} = \alpha + \gamma\lambda/(2 + 3\lambda) + O[(a/H)^3]$, with the note that the $O[(a/H)^3]$ contribution emerges from the consideration of wall effects. Using the method of reflection, theoretically it is possible to obtain the wall effects which provide the correction $I_1 + I_4/2 = O[(a/H)^3]$ [11].

Now, starting from Eq. (23), the oscillating flow condition ($\varepsilon_1 = 0, \varepsilon_2 = 1$) implies

$$u_{dx}^{(0)} \propto \sin(t\,\mathrm{St}). \tag{24}$$

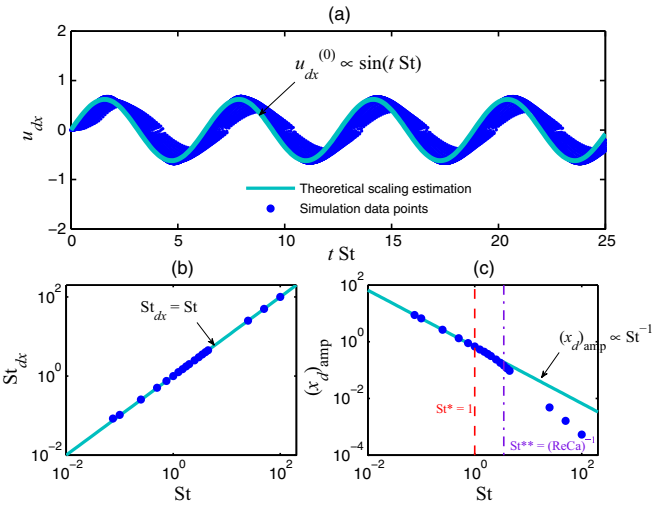

FIG. 12. Comparison of the present simulation results on the streamwise migration characteristics with the $O(1)$ theoretical approximation. In the figure, the markers represent the simulation data points while the solid lines represent the theoretical approximations. Note that the light shaded band appearing in the u_{dx} characteristics are the markers representing simulation data points over a wide range of St. Here the simulation data are taken for $a/H = 0.4375$ and $\mathrm{Ca} = 0.286$.

Subsequently, we have

$$x_d \propto \int \sin(t\,\mathrm{St})dt \Rightarrow x_d \propto \frac{1}{\mathrm{St}}\cos(t\,\mathrm{St}). \tag{25}$$

Figure 12(a) shows that the present scaling notion [Eqs. (24) and (25)] gives fairly good agreement with the simulation results, at least for describing the time complexity of u_{dx}. Through the analysis of Lissajous-like patterns (cf. Fig. 9) we predict the sinusoidal pattern of u_{dx}. The theoretical estimation through Eq. (24) verifies the ansatz. In tune with Eq. (24), we have $\mathrm{St}_{dx} = \mathrm{St}$ [Fig. 12(b)], with St_{dx} being the frequency of oscillation in u_{dx}. Subsequently, from Eq. (25) we obtain the relation $(x_d)_{\mathrm{amp}} \propto \mathrm{St}^{-1}$ [Fig. 12(c)], with $(x_d)_{\mathrm{amp}}$ being the amplitude of x_d. This inverse relationship between $(x_d)_{\mathrm{amp}}$ and St explains the difference in the $x_d - \theta$ patterns at different St, as already emphasized in Fig. 8. Note that here the simulation data are taken for $a/H = 0.4375$ and $\mathrm{Ca} = 0.286$, to highlight the features for confined droplets.

However, from Fig. 12, we note the departure of the simulation results from the present scaling notion [Eqs. (24) and (25)]. This is attributed to the increased difference between the droplet response time scale and the time scale of alteration in the flow field, at higher St. From the time scale analysis presented in Sec. IV, we note two important facts. First, at $\mathrm{St} > 1$, transportation is impeded as the time of alteration of the time periodic frequency is much longer than the time required to transport. Second, drop shape modification takes place when $\mathrm{St} \leqslant (\mathrm{ReCa})^{-1}$, allowing time for shape adjustment in response to the time scale of alteration of imposed forcing. In Fig. 12, we indicate the limits $\mathrm{St}^* = 1$ and $\mathrm{St}^{**} = (\mathrm{ReCa})^{-1}$. From the figure it is evident that the difference between simulation results and scaling theory is pronounced beyond the limiting Strouhal numbers, as predicted by the scaling arguments.

D. Effect of inertia due to imposed time complexity: the $O(\mathrm{Re})$ problem

The governing equations for the $O(\mathrm{Re})$ problem are

$$\left.\begin{aligned}
&\text{(a)}\ \nabla\cdot\mathbf{u}^{(\mathrm{Re})} = 0 \quad \text{and} \quad \nabla\cdot\mathbf{T}^{(\mathrm{Re})} = \frac{\partial\mathbf{u}^{(0)}}{\partial t} + \mathbf{u}^{(0)}\cdot\nabla\mathbf{u}^{(0)} \\
&\qquad\qquad \text{with} \quad \mathbf{T}^{(\mathrm{Re})} = -p^{(\mathrm{Re})}\mathbf{I} + \{\nabla\mathbf{u}^{(\mathrm{Re})} + (\nabla\mathbf{u}^{(\mathrm{Re})})^T\}, \\
&\text{(b)}\ \nabla\cdot\bar{\mathbf{u}}^{(\mathrm{Re})} = 0 \ \text{and} \ \nabla\cdot\bar{\mathbf{T}}^{(\mathrm{Re})} = \frac{\partial\bar{\mathbf{u}}^{(0)}}{\partial t} + \bar{\mathbf{u}}^{(0)}\cdot\nabla\bar{\mathbf{u}}^{(0)} \\
&\qquad\qquad \text{with} \quad \bar{\mathbf{T}}^{(\mathrm{Re})} = -\lambda\bar{p}^{(\mathrm{Re})}\mathbf{I} + \lambda\{\nabla\bar{\mathbf{u}}^{(\mathrm{Re})} + (\nabla\bar{\mathbf{u}}^{(\mathrm{Re})})^T\}, \\
&\text{(c)}\ \nabla\cdot\mathbf{u}_\infty^{(\mathrm{Re})} = 0 \ \text{and} \ \nabla\cdot\mathbf{T}_\infty^{(\mathrm{Re})} = \frac{\partial\bar{\mathbf{u}}_\infty^{(0)}}{\partial t} + \bar{\mathbf{u}}_\infty^{(0)}\cdot\nabla\bar{\mathbf{u}}_\infty^{(0)} \\
&\qquad\qquad \text{with} \quad \mathbf{T}_\infty^{(\mathrm{Re})} = -p_\infty^{(\mathrm{Re})}\mathbf{I} + \left\{\nabla\mathbf{u}_\infty^{(\mathrm{Re})} + \left(\nabla\mathbf{u}_\infty^{(\mathrm{Re})}\right)^T\right\},
\end{aligned}\right\} \tag{26}$$

with the boundary and interfacial conditions

$$\left.\begin{aligned}
&\text{(i)}\ \mathbf{u}^{(\mathrm{Re})} \to \mathbf{u}_\infty^{(\mathrm{Re})} \ \text{as} \ r \to \infty, \\
&\text{(ii)}\ \mathbf{u}^{(\mathrm{Re})} = -\mathbf{u}_d^{(\mathrm{Re})} \ \text{on the walls}, \\
&\text{(iii)}\ \mathbf{u}^{(\mathrm{Re})} = \bar{\mathbf{u}}^{(\mathrm{Re})} \ \text{at} \ r = 1, \\
&\text{(iv)}\ \mathbf{u}^{(\mathrm{Re})}\cdot\hat{\mathbf{e}}_r = \bar{\mathbf{u}}^{(\mathrm{Re})}\cdot\hat{\mathbf{e}}_r = 0 \ \text{at} \ r = 1, \quad \text{and} \\
&\text{(v)}\ \mathbf{T}^{(\mathrm{Re})}\cdot\hat{\mathbf{e}}_r - \bar{\mathbf{T}}^{(\mathrm{Re})}\cdot\hat{\mathbf{e}}_r = -[2f^{(\mathrm{ReCa})} + \nabla^2 f^{(\mathrm{ReCa})}]\hat{\mathbf{e}}_r \quad \text{at} \quad r = 1.
\end{aligned}\right\} \tag{27}$$

Subsequently, the reciprocal identity [Eq. (15)] transforms to

$$\begin{aligned}
&\int_{S_d}\left[(\mathbf{T}^{(\mathrm{Re})} - \bar{\mathbf{T}}^{(\mathrm{Re})})\cdot\mathbf{u}_c - (\mathbf{T}_c - \bar{\mathbf{T}}_c)\cdot\mathbf{u}^{(\mathrm{Re})} - \bar{\mathbf{T}}_c\cdot(\mathbf{u}^{(\mathrm{Re})} - \bar{\mathbf{u}}^{(\mathrm{Re})}) \quad - \mathbf{T}_\infty^{(\mathrm{Re})}\cdot\mathbf{u}_c + \mathbf{T}_c\cdot\mathbf{u}_\infty^{(\mathrm{Re})}\right]\cdot\hat{\mathbf{e}}_r dS \\
&= -\left\{\int_\Omega\left[\left(\frac{\partial\mathbf{u}^{(0)}}{\partial t} + \mathbf{u}^{(0)}\cdot\nabla\mathbf{u}^{(0)}\right) - \left(\frac{\partial\mathbf{u}_\infty^{(0)}}{\partial t} + \mathbf{u}_\infty^{(0)}\cdot\nabla\mathbf{u}_\infty^{(0)}\right)\right]\cdot\mathbf{u}_c d\Omega - \int_\Omega\left[\frac{\partial\bar{\mathbf{u}}^{(0)}}{\partial t} + \bar{\mathbf{u}}^{(0)}\cdot\nabla\bar{\mathbf{u}}^{(0)}\right]\cdot\bar{\mathbf{u}}_c d\Omega\right\}.
\end{aligned} \tag{28}$$

From the reciprocal identity [Eq. (28)], it is evident that we require the $O(\mathrm{Re})$ solution of the imposed flow field. This degenerates to the form

$$\mathbf{u}_\infty^{(\mathrm{Re})} = \left[\frac{\alpha}{2}(\psi^2 + \alpha') + \frac{\beta}{6}(\psi^3 + \beta') + \frac{\gamma}{12}(\psi^4 + \gamma')\right]\dot{\Gamma}(t)\hat{\mathbf{e}}_\xi - \frac{y_d}{2a/H}\dot{\mathbf{u}}_d^{(0)} - \mathbf{u}_d^{(\mathrm{Re})}, \tag{29}$$

with $\alpha' = s[(a/H)^{-1} - y_d]$, $\beta' = 2y_d[(a/H)^2 - y_d^2]/3$, $\gamma' = 6y_d[(a/H)^{-3} - y_d^3]$, and the dots represent the time derivative. Additionally, we require the solution of the complementary problem. Without any loss of generality, we can adopt the solution from Ref. [11].

With the above mentioned arguments through Eqs. (26)–(29), we eventually end up with the relation

$$u_{dy}^{(\mathrm{Re})} = \chi_1' u_{dx}^{(\mathrm{Re})} + \chi_2' u_{dx}^{(0)} + \chi_3'\dot{u}_{dx}^{(0)} + \chi_4'\dot{\Gamma}(t) + \chi_5', \tag{30}$$

where the coefficients χ' can be obtained from the reciprocal identity [Eq. (28)], using the $O(1)$ solutions for the entire problem and the $O(\mathrm{Re})$ solution of the imposed flow field. Note that here we are interested in unveiling the time-complex features. Thus, the exact forms of χ's are not important here. In expressing $u_{dy}^{(\mathrm{Re})}$ through Eq. (30), all quantities are known except $u_{dx}^{(\mathrm{Re})}$. Without any loss of generality, we may invoke the matching condition $\mathbf{u}^{(\mathrm{Re})} \to \mathbf{u}_\infty^{(\mathrm{Re})}$ as $r \to \infty$ to approximate the temporal nature of $\mathbf{u}^{(\mathrm{Re})}$. The complete description of $\mathbf{u}^{(\mathrm{Re})}$, however, requires the $O(\mathrm{Re})$ level solution of the problem with proper accounting of the overlapping of the outer and the inner region. Restricting our attention to the analysis of time complexity, thus, from the force estimation we expect the nature of $u_{dx}^{(\mathrm{Re})}$ is of the form

$$u_{dx}^{(\mathrm{Re})} = \Xi_1 + \Xi_2 \dot{\Gamma}(t) + \Xi_3 \dot{u}_{dx}^{(0)}, \tag{31}$$

with Ξ's being the coefficients.

Now, using Eqs. (23) and (31) in Eq. (30), we obtain

$$u_{dy}^{(\mathrm{Re})} = \chi_1 + \chi_2 \Gamma(t) + \chi_3 \dot{\Gamma}(t), \tag{32}$$

with χ's being the new constants. Eq. (32) can be considered as the generic scaling estimation of $u_{dy}^{(\mathrm{Re})}$ to describe its time complexity.

E. Effect of deformation: the $O(\mathrm{Ca})$ problem

The governing equations for the $O(\mathrm{Ca})$ problem are

$$\left.\begin{aligned}
&\text{(a) } \nabla\cdot\mathbf{u}^{(\mathrm{Ca})} = 0 \quad \text{and} \quad \nabla\cdot\mathbf{T}^{(\mathrm{Ca})} = 0 \quad \text{with} \quad \mathbf{T}^{(\mathrm{Ca})} = -p^{(\mathrm{Ca})}\mathbf{I} + \{\nabla\mathbf{u}^{(\mathrm{Ca})} + (\nabla\mathbf{u}^{(\mathrm{Ca})})^T\},\\
&\text{(b) } \nabla\cdot\bar{\mathbf{u}}^{(\mathrm{Ca})} = 0 \quad \text{and} \quad \nabla\cdot\bar{\mathbf{T}}^{(\mathrm{Ca})} = 0 \quad \text{with} \quad \bar{\mathbf{T}}^{(\mathrm{Ca})} = -\lambda\bar{p}^{(\mathrm{Ca})}\mathbf{I} + \lambda\{\nabla\bar{\mathbf{u}}^{(\mathrm{Ca})} + (\nabla\bar{\mathbf{u}}^{(\mathrm{Ca})})^T\},\\
&\text{(c) } \nabla\cdot\mathbf{u}_\infty^{(\mathrm{Ca})} = 0 \quad \text{and} \quad \nabla\cdot\mathbf{T}_\infty^{(\mathrm{Ca})} = 0 \quad \text{with} \quad \mathbf{T}_\infty^{(\mathrm{Ca})} = -p_\infty^{(\mathrm{Ca})}\mathbf{I} + \left\{\nabla\mathbf{u}_\infty^{(\mathrm{Ca})} + \left(\nabla\mathbf{u}_\infty^{(\mathrm{Ca})}\right)^T\right\},
\end{aligned}\right\} \tag{33}$$

with the boundary and interfacial conditions

$$\left.\begin{aligned}
&\text{(i) } \mathbf{u}^{(\mathrm{Ca})} \to \mathbf{u}_\infty^{(\mathrm{Ca})} \text{ as } r \to \infty,\\
&\text{(ii) } \mathbf{u}^{(\mathrm{Ca})} = -\mathbf{u}_d^{(\mathrm{Ca})} \text{ on the walls,}\\
&\text{(iii) } \mathbf{u}^{(\mathrm{Ca})} + f^{(\mathrm{Ca})}\frac{\partial\mathbf{u}^{(0)}}{\partial r} = \bar{\mathbf{u}}^{(\mathrm{Ca})} + f^{(\mathrm{Ca})}\frac{\partial\bar{\mathbf{u}}^{(0)}}{\partial r} \text{ at } r = 1,\\
&\text{(iv) } \left[\mathbf{u}^{(\mathrm{Ca})} + f^{(\mathrm{Ca})}\frac{\partial\mathbf{u}^{(0)}}{\partial r}\right]\cdot\hat{\mathbf{e}}_r - \mathbf{u}^{(0)}\cdot\nabla f^{(\mathrm{Ca})} = \left[\bar{\mathbf{u}}^{(\mathrm{Ca})} + f^{(\mathrm{Ca})}\frac{\partial\bar{\mathbf{u}}^{(0)}}{\partial r}\right]\cdot\hat{\mathbf{e}}_r - \bar{\mathbf{u}}^{(0)}\cdot\nabla f^{(\mathrm{Ca})} = 0 \text{ at } r = 1, \text{ and}\\
&\text{(v) } \left[\mathbf{T}^{(\mathrm{Ca})} + f^{(\mathrm{Ca})}\frac{\partial\mathbf{T}^{(0)}}{\partial r}\right]\cdot\hat{\mathbf{e}}_r - \left[\bar{\mathbf{T}}^{(\mathrm{Ca})} + f^{(\mathrm{Ca})}\frac{\partial\bar{\mathbf{T}}^{(0)}}{\partial r}\right]\cdot\hat{\mathbf{e}}_r - [\mathbf{T}^{(0)} - \bar{\mathbf{T}}^{(0)}]\cdot\nabla f^{(\mathrm{Ca})}\\
&\qquad = [2f^{(\mathrm{Ca})} + \nabla^2 f^{(\mathrm{Ca})}]\nabla f^{(\mathrm{Ca})} - [2f^{(\mathrm{CaCa})} - 2f^{(\mathrm{Ca})}f^{(\mathrm{Ca})} + \nabla^2 f^{(\mathrm{CaCa})}]\hat{\mathbf{e}}_r \quad \text{at} \quad r = 1.
\end{aligned}\right\} \tag{34}$$

Subsequently, the reciprocal identity [Eq. (15)] transforms to

$$\int_{S_d}\left[(\mathbf{T}^{(\mathrm{Ca})} - \bar{\mathbf{T}}^{(\mathrm{Ca})})\cdot\mathbf{u}_c - (\mathbf{T}_c - \bar{\mathbf{T}}_c)\cdot\mathbf{u}^{(\mathrm{Ca})} - \bar{\mathbf{T}}_c\cdot(\mathbf{u}^{(\mathrm{Ca})} - \bar{\mathbf{u}}^{(\mathrm{Ca})}) - \mathbf{T}_\infty^{(\mathrm{Ca})}\cdot\mathbf{u}_c + \mathbf{T}_c\cdot\mathbf{u}_\infty^{(\mathrm{Ca})}\right]\cdot\hat{\mathbf{e}}_r dS = 0. \tag{35}$$

Now we approximate different integrals using the matching conditions from Eq. (34) [11]:

$$\begin{aligned}
&\text{(i) } \int_{S_d}[(\mathbf{T}^{(\mathrm{Ca})} - \bar{\mathbf{T}}^{(\mathrm{Ca})})\cdot\mathbf{u}_c\cdot\hat{\mathbf{e}}_r dS = \int_{S_d}\Big[-f^{(\mathrm{Ca})}\frac{\partial}{\partial r}(\mathbf{T}^{(0)} - \bar{\mathbf{T}}^{(0)})\cdot\hat{\mathbf{e}}_r + (\mathbf{T}^{(0)} - \bar{\mathbf{T}}^{(0)})\cdot\nabla f^{(\mathrm{Ca})}\\
&\qquad\qquad + (2f^{(\mathrm{Ca})} + \nabla^2 f^{(\mathrm{Ca})})\nabla f^{(\mathrm{Ca})}\Big]\cdot\mathbf{u}_c dS\\
&\text{(ii) } -\int_{S_d}(\mathbf{T}_c - \bar{\mathbf{T}}_c)\cdot\mathbf{u}^{(\mathrm{Ca})}\cdot\hat{\mathbf{e}}_r dS = \int_{S_d}(\mathbf{T}_c - \bar{\mathbf{T}}_c) : \hat{\mathbf{e}}_r\hat{\mathbf{e}}_r\left[f^{(\mathrm{Ca})}\frac{\partial\mathbf{u}^{(0)}}{\partial r}\cdot\hat{\mathbf{e}}_r - \mathbf{u}^{(0)}\cdot\nabla f^{(\mathrm{Ca})}\right]dS\\
&\text{(iii) } -\int_{S_d}\bar{\mathbf{T}}_c\cdot(\mathbf{u}^{(\mathrm{Ca})} - \bar{\mathbf{u}}^{(\mathrm{Ca})})\cdot\hat{\mathbf{e}}_r dS = \int_{S_d}\bar{\mathbf{T}}_c\cdot\hat{\mathbf{e}}_r\cdot\left[f^{(\mathrm{Ca})}\frac{\partial}{\partial r}(\mathbf{u}^{(0)} - \bar{\mathbf{u}}^{(0)})\right]dS\\
&\text{(iv) } \int_{S_d}\left[-\mathbf{T}_\infty^{(\mathrm{Ca})}\cdot\mathbf{u}_c + \mathbf{T}_c\cdot\mathbf{u}_\infty^{(\mathrm{Ca})}\right]\cdot\hat{\mathbf{e}}_r dS = -2\pi\frac{2+3\lambda}{1+\lambda}(1 + J_1 + J_4)u_{dy}^{(\mathrm{Ca})},
\end{aligned} \tag{36}$$

where J_1 and J_4 have the same meaning as in Ref. [11].

From Eq. (36), it is evident that for estimating $u_{dy}^{(\mathrm{Ca})}$, we need to have the $O(1)$ solution and estimation of $f^{(\mathrm{Ca})}$. The later can be estimated using the matching condition from Eq. (21),

$$\mathbf{T}^{(0)} \cdot \hat{\mathbf{e}}_r - \bar{\mathbf{T}}^{(0)} \cdot \hat{\mathbf{e}}_r = -[2f^{(\mathrm{Ca})} + \nabla^2 f^{(\mathrm{Ca})}]\hat{\mathbf{e}}_r \text{ at } r = 1. \quad (37)$$

Now, introducing the $O(1)$ solution, it is sufficient to consider $(\mathbf{T}^{(0)} \cdot \hat{\mathbf{e}}_r - \bar{\mathbf{T}}^{(0)} \cdot \hat{\mathbf{e}}_r) \propto \Gamma(t)$. In tune with the matching condition [Eq. (37)], thus, we can approximate that $f^{(\mathrm{Ca})} \propto \Gamma(t)$. If we consider the integrals in Eq. (36), they are of the form $\int_{S_d} f^{(\mathrm{Ca})} \cdot \mathbf{T}^{(0)} \cdot \hat{\mathbf{e}}_r$ or $\int_{S_d} f^{(\mathrm{Ca})} \cdot \mathbf{u}^{(0)} \cdot \hat{\mathbf{e}}_r$. Invoking the estimation $f^{(\mathrm{Ca})} \propto \Gamma(t)$, $\mathbf{u}^{(0)} \propto \Gamma(t)$, and $\mathbf{T}^{(0)} \propto \Gamma(t)$, thus, we can represent $u_{dy}^{(\mathrm{Ca})}$ as

$$u_{dy}^{(\mathrm{Ca})} = \Pi_1 + \Pi_2 \Gamma(t)^2, \quad (38)$$

with Πs being the coefficients.

F. Combined influence of inertia and deformation on the time complexity of the lateral movement

To introduce the combined influence of inertia and deformation, to the leading order approximation, it is sufficient to recall the $O(\mathrm{Re})$ and $O(\mathrm{Ca})$ approximation of u_{dy}, as

$$\begin{aligned} u_{dy} &= \mathrm{Re}u_{dy}^{(\mathrm{Re})} + \mathrm{Ca}u_{dy}^{(\mathrm{Ca})} + \cdots \\ &= \mathrm{Re}[\chi_1 + \chi_2\Gamma(t) + \chi_3\dot{\Gamma}(t)] + \mathrm{Ca}[\Pi_1 + \Pi_2\Gamma(t)^2] + \cdots . \end{aligned} \quad (39)$$

Introducing $\Gamma(t) = \varepsilon_1 + \varepsilon_2 \sin(t\mathrm{St})$, Eq. (39) can be given by

$$\begin{aligned} u_{dy} &= \mathrm{Re}[\chi_1 + \chi_2\{\varepsilon_1 + \varepsilon_2 \sin(t\mathrm{St})\} + \chi_3\varepsilon_2\mathrm{St}\cos(t\mathrm{St})] \\ &\quad + \mathrm{Ca}\big[\Pi_1 + \Pi_2\big\{\varepsilon_1^2 + \varepsilon_2^2\sin^2(t\mathrm{St}) \\ &\quad + 2\varepsilon_1\varepsilon_2 \sin(t\mathrm{St})\big\}\big] + \cdots . \end{aligned} \quad (40)$$

For an oscillating flow condition ($\varepsilon_1 = 0, \varepsilon_2 = 1$), Eq. (40) yields

$$\begin{aligned} u_{dy} &= \mathrm{Re}[\chi_1 + \chi_2 \sin(t\mathrm{St}) + \chi_3\mathrm{St}\cos(t\mathrm{St})] \\ &\quad + \mathrm{Ca}[\Pi_1 + \Pi_2\sin^2(t\mathrm{St})] + \cdots . \end{aligned} \quad (41)$$

Starting from Eq. (41), u_{dy} can be given by a scaling relationship of the form

$$u_{dy} = c_1 + c_2 \sin(t\mathrm{St}) + c_3\sin^2(t\mathrm{St}) + c_4\mathrm{St}\cos(t\mathrm{St}), \quad (42)$$

with c's being the coefficients. Equation (42) describes a generic scaling estimation for the time complexity of the lateral migration speed due to the imposed oscillation in the flow field. Figure 13 compares the scaling relationship in Eq. (42) with the present simulation results at different St. Note that here the simulation data are taken for $a/H = 0.4375$ and $\mathrm{Ca} = 0.286$, to highlight the features for confined droplets. It needs to be emphasized that Fig. 13 hints at the existence of a phase shift as well as the difference between simulation results and scaling theory. The theory is developed for $a/H \ll 1$, though the droplet is in a confined environment. However, the simulation results are presented for $a/H = 0.4375$ which is less than unity but not much less, in a strict sense. Thus, a difference is expected. Nevertheless, the comparison presented in Fig. 13 indicates that our theoretical analysis is sufficient to bring out the time complexity of dynamical features of a confined droplet in an oscillating flow field.

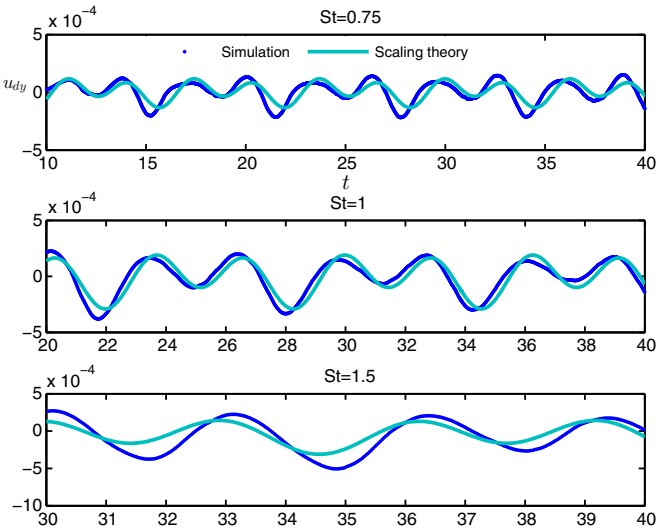

FIG. 13. Comparison of the present scaling estimation of the time complexity of u_{dy} with the simulation data points for different St. Here, the simulation data are taken for $a/H = 0.4375$ and $\mathrm{Ca} = 0.286$.

VI. SUGGESTED BENCHMARK FOR EXPERIMENTATION PURPOSES

The findings from our study are based on theoretical analysis (simulation, scaling, and analytical). A suggested benchmark for experimentation purposes, therefore, seems to be necessary. To this end, we would like to propose the following benchmarks:

(i) Observation of the helical pathway of a droplet in a time-complex flow field. For all practical purposes, the prevalence of a "time-complex" flow field is more likely rather than a harmonically oscillating flow, as we consider here. However, the dominant harmonics can be extracted from the time complexity. Subsequently, a helical pathway of the droplet is expected with respect to the dominant mode. Deviations from the expected pathway will portray the effects of other modes.

(ii) The Lissajous-like plots (Fig. 9) serve as the signature patterns for the interrelationships between the migration velocities and the temporal harmonics of the imposed forcing on the flow field. Estimation of the migration velocities of the droplet is expected to be an obvious endeavor in experiment. Using the results to construct Lissajous-like plots, as shown here, will unveil the signature characteristics for the situation of concern. These patterns will also help in developing an initial ansatz for the time complexities of the migration velocities, as we show here.

Experimentation with moving droplets and bubbles through a microchannel is common [44,53,56,57]. In addition to those approaches, a temporally varying flow field needs to be applied for observing the above mentioned features. To this end, various mechanical, electrical, and magnetic pumping systems can be favorable alternatives to generate harmonic unsteady flows (cf. Refs. [58–63] for details on microchannel pumping technologies). Furthermore, elastic-wave-induced secondary oil recovery is shown to be a promising technology in terms of enhanced recovery [24,63]. Thus, acoustic stimulation of droplets within a microconfinement can also be a relevant option. It is important to mention that most of the droplet based microfluidic systems are integrated with droplet generation units. A recent study shows the possibility of generating droplet on demand by controlled pulsating inlet pressures [62]. A microfluidic channel operating in conjunction with this droplet generating unit would be of immense technological significance with respect to which one can find a direct correspondence with our study.

VII. CONCLUSIONS

A. Summary of the findings

We observe and analyze the dynamics of a droplet within a parallel plate confinement subjected to a temporally oscillating flow field parallel to the channel walls. The prime focus of our study is to explore the pathway (along both axial and transverse directions) that the droplet follows in response to the time-complex flow field. We analyze the situation for a density and viscosity matched system; thus, all the conclusions are based on this criterion. Phase field simulations, scaling analysis, and concurrent theoretical analysis using a reciprocal identity based paradigm lead us to the following consensuses:

(a) The droplet follows a helical pathway in a sinusoidal flow field, which is characterized by a dimensionless frequency (St). The direction of the motion is towards the channel centerline.

(b) At low St, the pathway closely approximates that under a plane Poiseuille flow condition. However, an axial oscillation can be noted upon reaching the channel centerline which is the transverse equilibrium position.

(c) Upon increase in St, departure from the pathway under a plane Poiseuille flow condition is noted, along with the prevalence of a prominent helical pathway. Interestingly, we observe a net transverse displacement with almost zero net axial displacement at higher St. However, transverse displacement is also impeded considerably at higher St.

(d) The incipient hydrodynamics depends on the multiple time scales involved. In particular, their relative importance sets in the guiding principles for the resulting phenomenological features. Corresponding scaling analysis shows that transportation is impeded for $\mathrm{St} > 1$, and shape adjustment of the droplet is disrupted for $\mathrm{St} > (\mathrm{ReCa})^{-1}$.

(e) Analysis of the simulation results and the reciprocal based theoretical analysis put our observations in a quantitative perspective. The time complexities of the migration speed of the droplet are found to be of the forms (axial) $u_{dx} = \Lambda_{\mathrm{CL}} \sin(t\mathrm{St})$ and (transverse) $u_{dy} = c_1 + c_2 \sin(t\mathrm{St}) + c_3 \sin^2(t\mathrm{St}) + c_4 \mathrm{St} \cos(t\mathrm{St})$ [cf. Eqs. (23) and (42) for details]. These estimations further quantify the amplitudes and frequencies of the time-complex axial and transverse migratory characteristics of the droplet.

B. Remarks

Our observations and analyses are based on various possible state-of-the-art fundamental approaches. Specifically, we wish to develop an integrated consensus, supported by possible fundamental doctrines. In this respect, as we believe, our study adds to the fundamental understanding. However, several issues need to be taken into consideration while interpreting the results of the present study, which also open up possible sources of future research questions.

Though the numerical intricacies of the phase field model have a corresponding thermodynamic genesis, several unavoidable issues, such as droplet mass shrinkage, divergence from a sharp interface limit, require numerical management. We adopt the previously established guidelines to validate and assess our model setup. However, we need to endeavor to make an extension of the established guidelines for time-complex two-phase flows. Specifically, the hydrodynamics of a time-complex flow field is guided by the multiple physics occurring over multiple time scales. Overlapping of those multiphysics with the inherent physics of the phase field model is expected to insinuate various phenomenological and numerical features which would be an interesting topic of research.

We present a reciprocal identity based theoretical analysis to unveil the time complexities of the droplet motion. A comprehensive understanding, however, requires an estimation of the spatiotemporal complexities of the droplet motion. Furthermore, the theoretical analysis is based on a small droplet approximation. Improvement of the theoretical model considering larger size droplets within a confinement is suggested as a scope of further study. Another important aspect that can be considered in future studies is the effect of Re on the drop dynamics. This brings in the contributions of inertia on the droplet dynamics where the inertia is brought about by the temporally varying flow field.

APPENDIX: GRID INDEPENDENT AND Cn INDEPENDENT STUDY

To perform a grid independent study, we consider the temporal evolution of the migration characteristics $[x_d(t), y_d(t), u_{dx}(t), \text{and } u_{dy}(t)]$ at $\mathrm{St} = 1, a/H = 0.4375, \mathrm{Ca} = 0.286$, and $\mathrm{Re} = 1$ for different grid sizes, as shown in Fig. 14. In diffuse interface methods like phase field, the numerical results should be independent of the interfacial thickness which is represented by the Cahn number (Cn). To make the results Cn independent, we consider different values of Cn as well. We find that the numerical setup with $\mathrm{Cn} = 0.02$ and $\Delta x = 0.01$ is sufficient for the present analysis, taking accuracy and computational expenses into combined consideration. Regarding the choice of Pe, we consider $\mathrm{Pe} = 10^6$ which gives constant interface thickness.

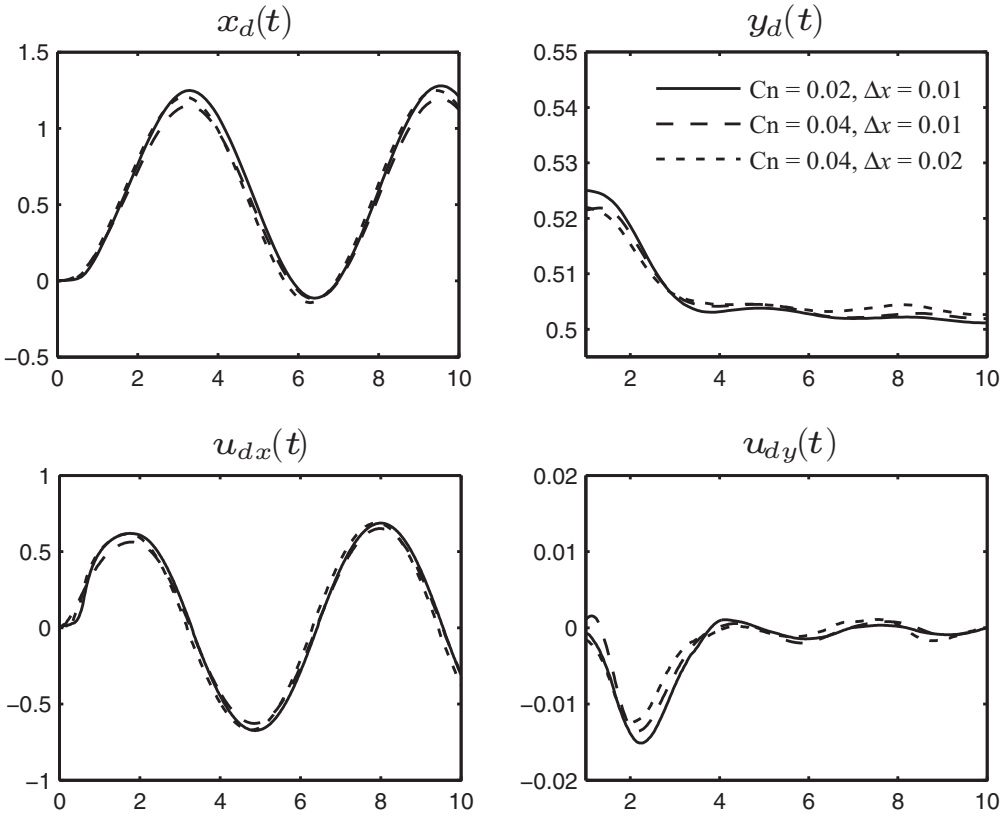

FIG. 14. Grid and Cn independent test for the migration characteristics of a droplet with $a/H = 0.4375$, Re $= 1$, and Ca $= 0.286$, in an oscillating flow field at St $= 1$. The figure also demonstrates a comparison between the different numerical setups, as decided by the combinations of Cn and Δx.

[1] X. Casadevall i Solvas and A. deMello, Chem. Commun. (Cambridge, U. K.) **47**, 1936 (2011).
[2] T. Schneider, J. Kreutz, and D. T. Chiu, Anal. Chem. **85**, 3476 (2013).
[3] H. A. Stone, A. D. Stroock, and A. Ajdari, Annu. Rev. Fluid Mech. **36**, 381 (2004).
[4] S.-Y. Teh, R. Lin, L.-H. Hung, and A. P. Lee, Lab Chip **8**, 198 (2008).
[5] L. Capretto, W. Cheng, M. Hill, and X. Zhang, Top. Curr. Chem. **304**, 27 (2011).
[6] S. Afkhami, A. M. Leshansky, and Y. Renardy, Phys. Fluids **23**, 022002 (2011).
[7] A. Carlson, M. Do-Quang, and G. Amberg, Int. J. Multiphase Flow **36**, 397 (2010).
[8] C. Chung, M. Lee, K. Char, K. H. Ahn, and S. J. Lee, Microfluid. Nanofluid. **9**, 1151 (2010).
[9] E. De Leo, L. Galluccio, A. Lombardo, and G. Morabito, *2012 IEEE International Conference on Communications (ICC)* (IEEE, Ottawa, 2012).
[10] D. A. Sessoms, M. Belloul, W. Engl, M. Roche, L. Courbin, and P. Panizza, Phys. Rev. E **80**, 016317 (2009).
[11] P. C.-H. Chan and L. G. Leal, J. Fluid Mech. **92**, 131 (1979).
[12] P. C.-H. Chan and L. G. Leal, J. Fluid Mech. **82**, 549 (1977).
[13] L. G. Leal, Annu. Rev. Fluid Mech. **12**, 435 (1980).
[14] X. Li and C. Pozrikidis, Phys. Fluids **14**, 61 (2002).
[15] S. Mortazavi and G. Tryggvason, J. Fluid Mech. **411**, 325 (2000).
[16] S. Mukherjee and K. Sarkar, J. Fluid Mech. **727**, 318 (2013).
[17] L. G. Leal, *Advanced Transport Phenomena* (Cambridge University Press, New York, 2007).
[18] K. Sarkar and W. R. Schowalter, J. Fluid Mech. **436**, 177 (2001).
[19] K. Sarkar and W. R. Schowalter, J. Fluid Mech. **436**, 207 (2001).
[20] X. Li and K. Sarkar, Phys. Fluids **17**, 027103 (2005).
[21] D. R. Graham and J. J. L. Higdon, J. Fluid Mech. **425**, 55 (2000).
[22] P. M. Lovalenti and J. F. Brady, Phys. Fluids **5**, 2104 (1993).
[23] J. Magnaudet, J. Fluid Mech. **485**, 115 (2003).
[24] D. R. Graham and J. J. L. Higdon, J. Fluid Mech. **425**, 31 (2000).
[25] F. Wilfling, J. T. Haas, T. C. Walther, and R. V. F. Jr, Curr. Opin. Cell Biol. **29**, 39 (2014).
[26] P. M. Vlahovska, T. Podgorski, and C. Misbah, C. R. Phys. **10**, 775 (2009).
[27] A. R. Thiam, R. V Farese, and T. C. Walther, Nat. Rev. Mol. Cell Biol. **14**, 775 (2013).
[28] V. E. Badalassi, H. D. Ceniceros, and S. Banerjee, J. Comput. Phys. **190**, 371 (2003).
[29] R. Borcia and M. Bestehorn, Phys. Rev. E **67**, 066307 (2003).
[30] D. M. Anderson, G. B. McFadden, and A. A. Wheeler, Annu. Rev. Fluid Mech. **30**, 139 (1998).
[31] D. Jacqmin, J. Comput. Phys. **155**, 96 (1999).
[32] H. Ding, P. D. M. Spelt, and C. Shu, J. Comput. Phys. **226**, 2078 (2007).

[33] H. Ding, M. N. H. Gilani, and P. D. M. Spelt, J. Fluid Mech. **644**, 217 (2010).
[34] J. Happel and H. Brenner, *Low Reynolds Number Hydrodynamics* (Springer Netherlands, Dordrecht, 1981).
[35] A. Nourbakhsh, S. Mortazavi, and Y. Afshar, Phys. Fluids **23**, 123303 (2011).
[36] A. J. Griggs, A. Z. Zinchenko, and R. H. Davis, Int. J. Multiphase Flow **33**, 182 (2007).
[37] F. Magaletti, F. Picano, M. Chinappi, L. Marino, and C. M. Casciola, J. Fluid Mech. **714**, 95 (2013).
[38] P. Yue, J. J. Feng, C. Liu, and J. Shen, J. Fluid Mech. **515**, 293 (2004).
[39] P. Yue, C. Zhou, and J. J. Feng, J. Fluid Mech. **645**, 279 (2010).
[40] P. Yue, C. Zhou, J. J. Feng, C. F. Ollivier-Gooch, and H. H. Hu, J. Comput. Phys. **219**, 47 (2006).
[41] P. Yue, C. Zhou, and J. J. Feng, J. Comput. Phys. **223**, 1 (2007).
[42] S. V. Patankar, *Numerical Heat Transfer and Fluid Flow* (CRC Press, Boca Raton, FL, 1980).
[43] K. Stüben, J. Comput. Appl. Math. **128**, 281 (2001).
[44] C. A. Stan, L. Guglielmini, A. K. Ellerbee, D. Caviezel, H. A. Stone, and G. M. Whitesides, Phys. Rev. E **84**, 036302 (2011).
[45] M. J. Martinez and K. S. Udell, J. Fluid Mech. **210**, 565 (2006).
[46] S. Shu and N. Yang, Ind. Eng. Chem. Res. **52**, 11391 (2013).
[47] E. Lac and J. D. Sherwood, J. Fluid Mech. **640**, 27 (2009).
[48] H. Lan and D. B. Khismatullin, Int. J. Multiphase Flow **47**, 73 (2012).
[49] J. Magnaudet, S. Takagi, and D. Legendre, J. Fluid Mech. **476**, 115 (2003).
[50] Y. Wang and P. Dimitrakopoulos, Theor. Comput. Fluid Dyn. **26**, 361 (2011).
[51] F. P. Bretherton, J. Fluid Mech. **10**, 166 (1961).
[52] S. Guido and V. Preziosi, Adv. Colloid Interface Sci. **161**, 89 (2010).
[53] S. Jakiela, P. M. Korczyk, S. Makulska, O. Cybulski, and P. Garstecki, Phys. Rev. Lett. **108**, 134501 (2012).
[54] See Supplemental Material at http://link.aps.org/supplemental/10.1103/PhysRevE.93.023106 for the pathway that the centroid of a droplet follows in an oscillating flow field at St = 0.5 and 2, within a parallel plate confinement.
[55] M. Ahmadlouydarab, J. Azaiez, and Z. Chen, Phys. Rev. E **91**, 023002 (2015).
[56] C. A. Stan, A. K. Ellerbee, L. Guglielmini, H. A. Stone, and G. M. Whitesides, Lab Chip **13**, 365 (2013).
[57] M. J. Fuerstman, A. Lai, M. E. Thurlow, S. S. Shevkoplyas, H. A. Stone, and G. M. Whitesides, Lab Chip 7, 1479 (2007).
[58] C. J. Morris and F. K. Forster, Exp. Fluids **36**, 928 (2004).
[59] B. D. Iverson and S. V. Garimella, Microfluid. Nanofluid. **5**, 145 (2008).
[60] X. Wang, C. Cheng, S. Wang, and S. Liu, Microfluid. Nanofluid. **6**, 145 (2009).
[61] M. Nabavi, Microfluid. Nanofluid. **7**, 599 (2009).
[62] B.-U. Moon, S. G. Jones, D. K. Hwang, and S. Tsai, Lab Chip **15**, 2437 (2015).
[63] I. A. Beresnev and P. A. Johnson, Geophysics **59**, 1000 (1994).